Modelling and experimental validation of dynamic impact in 1:9 railway crossing panel

Ma, Yuewei; Mashal, AA; Markine, Valeri

DOI
10.1016/j.triboint.2017.09.036

Publication date
2018

Document Version
Accepted author manuscript

Published in
Tribology International

Modelling and experimental validation of dynamic impact in 1:9 railway crossing panel

Yuewei Ma, Abdul Ahad Mashal, Valeri L. Markine

Section of Railway Engineering, Faculty of Civil Engineering and Geosciences, Delft University of Technology, Stevinweg 1, 2628CN, Delft, The Netherlands.

Abstract

To improve the understanding of dynamic impact in 1:9 crossing panel, which is suffering from rapid surface degradation, detailed modelling and experimental studies are performed. A three-dimensional explicit finite element (FE) model of a wheel rolling over a crossing rail, that has an adaptive mesh refinement procedure coupled with two-dimensional geometrical contact analyses, is developed. It is demonstrated that this modelling strategy performs much better than the 'conventional' FE modelling approach. Also, the experimental validations show that the FE results agree reasonably well with the field measurements. Using the validated FE model, the tribological behaviour of contact surfaces is studied. The results indicate that the proposed modelling strategy is a promising tool for addressing the problems of wheel-crossing dynamic impact.

Keywords: Dynamic impact; Finite element model; Experimental validation; Switches and crossings.

1. Introduction

Switches & crossings (S&C, also called 'turnouts', See Figure 1) are key operating devices on the railway network to manage the traffic flow effectively. As one of the three major components (namely, switch, closure and crossing panels, See Figure 1a), the crossing panel is specially designed to enable the wheel successfully travelling from the wing rail to the nose rail or the other way around. By this means, the vehicles are capable of safely switching from through/diverging routes in either facing or trailing directions (See Figure 1a). However, due to the natural geometrical discontinuity of the rail and the resulting gaps at the transition region (See Figure 1a and Figure 1c), highly concentrated impact loads on the crossing rail are induced and amplified from the passing vehicles. These repeated high impact loads would lead to the rapid degradation of contact interfaces (e.g., accumulated plastic deformations) and/or the initiation of micro-cracks on the rail surface/subsurface. The small cracks might further deteriorate into the spalling damage (See Figure 1d) or even lead to the sudden fracture of the crossing rail. Nowadays, the Dutch railway network is severely suffering from these problems according to [1], where it has been reported that a typical crossing (e.g., the one shown in Figure 1b-d) needs to be repaired urgently every half year. Thus, the crossing panel is being one of the most maintenance demanding components in the Dutch railway infrastructure.

During the last decades, extensive research resources [1–16] have been devoted to the subject of dynamic impact at S&C for the purpose of finding effective strategies to address the aforementioned impact-induced problems. Usually, these dynamic impact problems are studied experimentally [2, 4, 5, 7] and/or numerically [1, 3, 8–16]. Both approaches

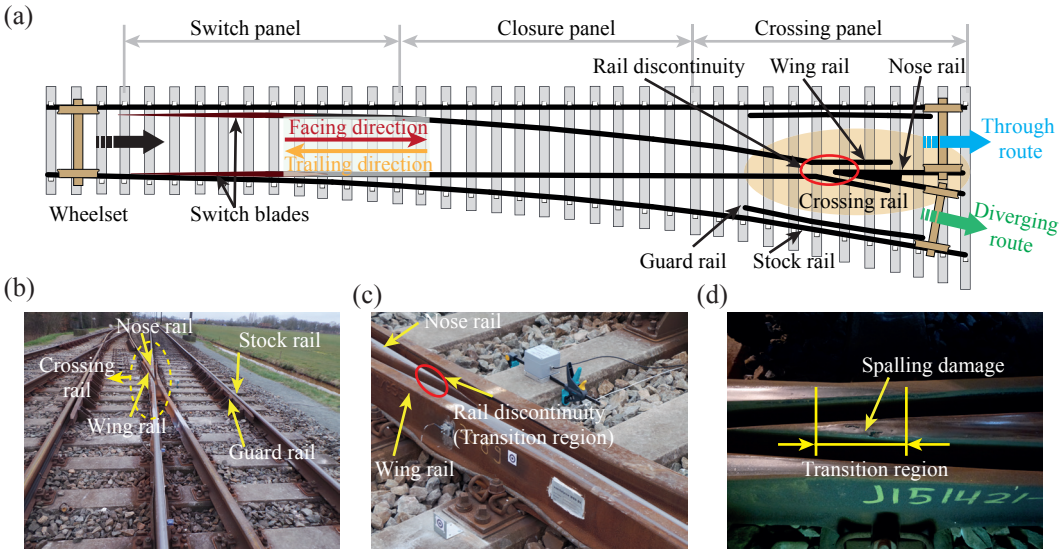

Figure 1: (a) Schematic of railway switches & crossings (adapted from [2], re-drawn by A. A. Mashal and then presented firstly in [3]); (b) 1:9 crossing panel on Dutch railway network (photo taken by V. Markine); (c) Close-up view of this crossing panel (photo taken by V. Markine); (d) Spalling damage on crossing nose (photo taken by Y. Ma).

are very helpful to improve the understanding of the dynamic impact phenomena. However, experimental studies are often time-consuming and considerably expensive [17]. As a consequence, the use of numerical simulations is much preferable, since it allows to repeat "experiments" easily [18], thus to assess the effect of all/selected parameters (e.g., operational, contact geometrical, track, vehicle parameters, etc.) on the performance of wheel-crossing (W/C) interaction separately/integrally [6, 9, 19–21], even to improve the local design of S&C contact geometry [1, 22, 23] or tune the elastic track properties through optimisation [10, 24, 25]. Among the aforementioned numerical simulations, Hertzian [26], non-Hertzian[27], multi-Hertzian [28] contact theories are often adopted for the calculation of normal contact forces, whereas fast and approximate frictional contact algorithms, such as FASTSIM [27], FASTSIM2 [29], Polach's method [30] and table-lookup schemes [27] are commonly used to get the tangential contact forces. These different types of normal/tangential contact models are well established and successfully integrated with many MBS(Multi-body Dynamic System) software (e.g., Adams VI-Rail, Vampire, Simpack, etc.). For the MBS simulations, all the components of vehicle & track are simplified/modelled as rigid bodies. The associated contact models are usually based on the assumptions of elastic (i.e., no material plasticity considered) half-space [27].

With the increase of expectations on the contact models for higher degree of realism and better accuracy, advanced computer programmes (such as CONTACT [27, 31], Finite Element (FE) method [32], etc.) are necessitated as alternatives for more detailed studies on the dynamic contact-impact phenomena [18]. Among the advanced numerical methods, the FE approach is more frequently used because of its striking versatility (i.e., the use of sophisticated elasto-plastic material models as well as the consideration of realistic/generic contact geometries). FE method, as opposed to the MBS method, is known as a powerful tool to determine the stresses/strains at the regions of interest with the assumption that the bodies are deformable. Yet, the FEM simulations usually demand more computational power than that of MBS due to the large number of elements discretized. During the last decades, the growing computer power and the development of computing techniques (i.e.,

parallel processing) significantly boost the FE modelling studies on the W/C dynamic impact. Thus, a number of pioneering research progresses [3, 11–13, 15, 16, 33, 34] have been made. For instance, Pletz et al. [11] were among the first to simulate the dynamic impact between a wheel and a full-scale crossing rail using explicit FE method. The effects of operational parameters (such as, train velocities, axle loads, etc.) on the behaviour of dynamic impact were studied thoroughly [11, 12]. The developed FE model was well verified against the MBS model. In [13], Wiest et al. developed a novel coupling procedure between MBS and FE programmes. Using that procedure, the full-scale W/C dynamic FE model was able to be simplified into a static sub-model with two small pieces (around 30 mm thick) of the contact bodies considered. The contact pressure was assessed and further compared with that of CONTACT analysis. In [16], Xin and Markine developed a complete FE model, in which both the full-scale wheel-set and the complete crossing panel were modelled. The accuracy of their model was evaluated through comparisons with the field measurements. Also, a thorough parametric study on the effect of major operational parameters (such as, axle loads, train velocities, etc.) on the dynamic impact phenomena was performed. In [33], Wei et al. presented a similar complete FE model. The simulated dynamic response was validated through comparisons with the in-situ measurements of axle box acceleration (ABA). A good agreement between the measured and simulated acceleration signals was found. The contact properties (e.g., normal pressure, shear stress, etc.) obtained were further used as an input to simulate the plastic deformation and wear on the surface of crossing rail. More recently, Wiedorn et al. [34] introduced a simplified finite element model for studying the impact of a wheel on a crossing. It was intended to improve the calculation efficiency of FE simulations by simplifying the contact geometries. The simulation results agreed reasonably well with the ones of full-scale FE model [11, 12].

In summary, the detailed knowledge on the W/C dynamic impact has been enhanced significantly with these various and valuable FE-based numerical studies (and experimental validations). Yet, there is still much work to be done to address the following issues:

- Demanding research on 1:9 crossing: Most of the aforementioned studies are focused on the impact phenomena of 1:15 crossing panels [11–13, 15, 16, 34]. Only few research interests [33] are in 1:9 crossing panel, which is currently suffering from stronger impact and rapider degradation (as described in Figure 1) than the one of 1:15, due to its bigger crossing angle ('1:n' is referred to as the crossing angle of the turnout, 'n' is also called the crossing number) and the reduced transition distance (i.e., the length of collateral running bands on the crossing rail, See Figure 1d). Also, the material (i.e., manganese steel) of 1:9 crossing rail is prone to the issues of surface degradation.

- Contact/impact-modelling difficulties: a) General challenges: Contact/impact always occurs at a priori unknown area until the problem is resolved. This unknown can bring about many challenges for the general cases of FE-based contact/impact modelling [35], such as the geometrical "gaps or penetrations", mismatched/insufficient mesh refinement, unexpected initial slips, etc. If these challenges are not addressed properly, the accuracy and efficiency of the corresponding FE simulations will be adversely affected [35]; b) Specific challenges: Regarding the modelling of W/C impact, the special modelling difficulties, such as, the 'discontinuous' mesh refinement, the prohibitive amount of elements & the low calculation efficiency, etc., are further increased due to the much complex local contact geome-

tries at the crossing panel. More details about these modelling difficulties/challenges will be given later in Section 2.1.2.

- Well-established experimental validations: Due to the complexity of W/C interaction and relatively small size of contact patches (around 150–200 mm^2, See [3]), it remains challenging to measure the local contact properties within the contact patches [36]. Therefore, well-established experimental validations for the presented FE-based contact models are still in high demand. Usually, the experimental devices (e.g. strain gauges, accelerometer, etc.) are instrumented onto the wheel, bogie, axle box (train-borne/on-board) [33, 37] or rail (track-side/wayside) [2–5, 16]. The acquired real-time strain/acceleration signals are preprocessed and then compared with the FE simulated results. By this means, the accuracy of the presented FE contact models is assessed indirectly [38]. However, these experimental validations are mostly focused on the single selected measurement instead of validating from the statistical/stochastic perspectives [6, 12]. In short, the problem of the experimental validations in terms of the FE-based contact models are still open to be addressed.

- Detailed stress/strain solutions of dynamic impact problems at S&C: It has been reported in [3, 11, 16] that the impact loadings will lead to the greatly increased contact stresses, which are far beyond the yield strength of typical steels. In reality, the accumulation of plastic deformation will manifest itself in the rather high levels of surface/subsurface damage (i.e., wear, RCF, etc.). To accurately quantify the wear/RCF resistance of typical materials and assess the long-term behaviour of S&C components, the detailed stress/strain solutions for this dynamic impact problem are, thus, practically needed. More discussion about the results of stress/strain will be presented in Section 4.

In order to enrich the detailed knowledge of W/C dynamic impact at 1:9 crossing panel, an explicit finite element model of a wheel rolling over a crossing rail is developed, which includes an effective and efficient modelling procedure through the coupling with two dimensional (2D) geometrical contact analyses [35]. Such a modelling strategy is originated and further extended from the authors' former work [35, 38, 39], which is focused on the normal wheel-rail interaction. The strategy (referred to as 'enhanced explicit FE-based coupling strategy', abbreviated as 'eFE-CS', hereinafter) has been described thoroughly in [35, 38, 39]. Its performance (refers to the accuracy, efficiency and flexibility) has been demonstrated through a number of numerical simulations with varying interface parameters and operational patterns [38, 39]. The effectiveness of this coupling strategy on addressing the general modelling challenges (such as 'gaps and/or penetrations', targeted mesh refinement, etc.) has been successfully proved. In this study, the approach on how to address both the general and specific modelling challenges of W/C dynamic impact is presented. Also, the performance of this extended 'eFE-CS' model is examined through the comparison with the 'conventional' FE modelling approach. Here, the 'conventional' means that the coupling strategy is not used.

As it is motivated to make this 'eFE-CS' contact model reliable and useful based on its own advantages, two procedures of experimental validations are introduced and described in this paper. The first procedure is based on the location of 'transition region' (See Figure 1d), which is referred to as the collateral zone of the two separate running bands. At this region, the change of wheel motion directly contributes to the subsequent impact responses according to [1]. The transition region has thus been suggested and used as an

indication of the potential damage locations on the crossing rail [9]. Considering the great importance of the transition region, it is inspired to compare the FE predicted transition region with the field measured ones, through which the accuracy of 'eFE-CS' model can be assessed.

On the other hand, the crossing accelerations induced by the impact event are collected by a real-time measuring system called ESAH-M (Elektronische System Analyse Herzstijckbereich – Mobil). Such a measurement device has been successfully used to monitor the structural health conditions of 1:15 crossing panel [4, 16]. For the studied 1:9 crossing panel, the measured accelerations are used to compare with those obtained from the FE simulations. To address the aforementioned open challenges of the experimental validations, the current validation is performed from a statistical perspective. A great number of measured acceleration signals (recorded from 21 train passages, around 400 W/C impacts) are collected and compared with the FE acceleration signal statistically both in the time and frequency domains. It shows that the modelling results agree reasonably well with the field measurements. Also, it implies that the presented 'eFE-CS' model can represent the real system of W/C interaction reasonably and is reliable & accurate enough to be used in the future work.

Using the validated 'eFE-CS' model, the corresponding FE results of the global dynamic contact forces as well as the detailed knowledge about the local surface contact properties (i.e., sliding-adhesion area, normal/shear stresses, etc.) within the contact patches are presented. At the same time, special research interests are focused on the subsurface stress responses. The relations between greatly increased contact stresses and the causes of rapid surface degradations are discussed.

The structure of this paper is as follows: In Section 2, the attention is focused on the general description of 3D FE model. Also, the specific modelling difficulties that prohibit an accurate solution of W/C dynamic impact are emphasized. The detailed working mechanisms of the coupling strategy are presented. The effectiveness of 'eFE-CS' model is assessed through a comparison with the 'conventional' FE model. In Section 3, experimental studies are performed to validate the accuracy of the proposed FE model. In Section 4, the results of surface and subsurface material responses obtained from the FE analysis are presented. The future work and further applications of the 'eFE-CS' model are discussed. Finally, concluding remarks are drawn.

2. Modelling of W/C impact

In this section, the modelling approach/strategy for the analyses of W/C dynamic impact is described. The two investigated counterparts are the standard S1002 wheel (EN13715 [40]) with a nominal rolling radius of 460mm and the 1:9 crossing rail (See Figure 1a-d and Figure 2a-c) used on a monitoring site near Meppel in the Netherlands.

The drawing of wheel cross-section is adopted from [41]. The inner gauge of the wheelset is 1360mm. The axle length is 2200mm. The crossing rail is cast of manganese steel and prefabricated as a single unit according to the standard drawing shown in Figure 2a-c. There is a group of characteristic cross-sections, ranging from AA to GG, specifically used to describe the whole crossing rail geometry. The overall length of this 1:9 crossing rail is 2950 mm. The nominal track gauge is 1435mm.

It can be seen from Figure 2a and Figure 2c that the lateral width of the wing rail head remains the same until CC cross-section. Then, it begins to shrink gradually in the lateral direction and stops at end of the wing rail (GG cross-section). For the nose rail (See Figure 2a-b), both the width (lateral) and height (vertical) of the rail head expand

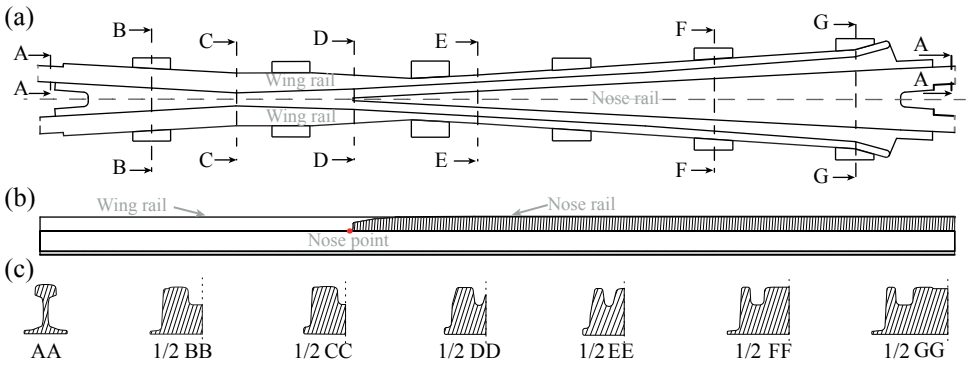

Figure 2: Drawing of crossing rail: (a) Global top view; (b)Vertical-longitudinal cross-sectional view; (c) Vertical-lateral cross-sectional view.

remarkably along the longitudinal path from DD to GG. Following that, it splits into two normal rails. At the two ends of the crossing rail, standard UIC54 normal rails(cross-section AA) are secured by stainless welds.

2.1. 3D W/C FE model

As a major component of the coupling strategy, the 3D W/C FE model is described firstly in Section 2.1.1. Following that, the reasons (mainly due to the FE modelling challenges) of adopting the 'eFE-CS' modelling strategy are explained in Section 2.1.2.

2.1.1. Model descriptions

A W/C FE model shown in Figure 3a-b is developed, where the crossing rail is modelled with restriction to an overall length of 7.45m. This finite length has been examined and confirmed in the previous research [3] that it is long enough to minimise the influence of the boundary conditions (at the two ends of the crossing rail) on the dynamic impact. The idea of constructing such a W/C FE model (single wheel considered) is inspired by the models described in [12, 36]. The global coordinate system O-XYZ is defined as: the Z-axis is parallel to the longitudinal direction along which the wheel-set travels, the Y-axis is the vertical pointing upwards, and the X-axis is perpendicular both Y and Z directions, forming a right-handed Cartesian coordinate system (See Figure 3a).

Only the solution regions where the wheel travels are discretized with fine mesh, leaving the remaining regions with coarse mesh. Here, the solution region (fine mesh area) is an area to extract and analyse the contact properties, such as the resulting contact patch, normal pressure, shear stress, etc. In this region, the mesh size is as small as 1.0mm (See Figure 3), which is prescribed for the purpose of capturing the accurate and high stress/strain gradients inside the contact patch. This mesh size (1.0mm) is 33% smaller than that of 1.33mm, which can ensure the good accuracy of contact solutions according to [36]. Moreover, the type of 3D 8-node brick (i.e., hexahedral) element (Solid164) with reduced (one point) integration is adopted so as to save the computational cost and enhance the robustness in cases of large deformations [42].

To take the primary suspension into account, a group of sprung mass blocks are lumped over the spring-damper system. The mass blocks, which are used to represent the weight of the loaded car body, are 10 tons. The substructures (i.e., rail-pad, ballast, etc.) are modelled as spring and damping elements as well. The sleepers are simplified by mass elements. The wheel and crossing rail are of the same material, which is considered to be bilinear isotropic hardening in ANSYS [43]. The values of the material/mechanical

.

Table 1: Material properties and mechanical parameters.

	Properties	Values
Wheel/rail material [a]	Young modulus(GPa)	210
	Tangent modulus(GPa)	21
	Yield strength (MPa)	480
	Possion ratio	0.3
	Density (kg/m^3)	7900
Primary suspension	Stiffness (MN/m)	1.15
	Damping (Ns/m)	2500
Operational parameters	Coefficient of friction [b]	0.5
	Coefficient of traction [c]	0.25
	Train velocities (km/h)	140
	Lateral displacement (mm)	0.0
Sleeper	Mass(kg)	244
Rail pad	Stiffness (MN/m)	1300
	Damping (kNs/m)	45
Ballast	Stiffness (MN/m)	45
	Damping (kNs/m)	32

[a]: Bilinear (elasto-plastic) isotropic hardening law, more information about this model can be found in [38].
[b]: Friction is the force resisting the relative motion (i.e., slip) of contact surfaces. Coefficient of friction = Friction force/Normal force. [c]: Traction is the force applied to generate motion between a body and a tangential surface. The tangential traction appears only if the friction is assumed. Coefficient of traction = Traction/Normal force.

parameters are listed in Table 1. The position of the sleepers (60cm spacing) follows the schematic shown in Figure 3a.

The wheel is set to roll on the crossing rail from the origin of the global coordinate system O-XYZ over a short travelling distance of 1.2m (See Figure 3a), which is long enough to ensure that the wheel can travel over the transition region completely. The initial train speed is 140km/h. The rotations of the wheel around the Y-axis are disabled (i.e., turned off or prevented from occurring), since it is assumed that variations of the wheel-set's yaw angles are small over a short rolling distance (i.e., 1.2m).

To better simulate the W/C dynamic impact process, an implicit-to-explicit sequential solving procedure [42] is used. In this procedure, the implicit solver(ANSYS Mechanical) and explicit solver (ANSYS LS-DYNA) work in pairs. First, the equilibrium state of the preloaded structure (i.e., axle-load 100kN applied) is determined with ANSYS Mechanical. The displacement results of the implicit analysis are adopted to do a stress initialization for the subsequent transient analysis. Then, the dynamic impact processes begin at time zero with a stable preloaded structure [43]. The impact responses are further simulated with ANSYS LS-DYNA using the central difference time integration scheme [42]. Also, double precision LS-DYNA [42] is used so as to ensure good accuracy of the contact solutions.

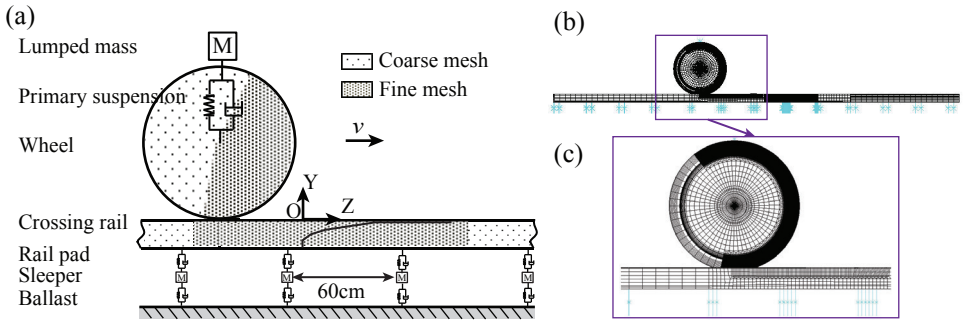

Figure 3: Explicit FE model of W/C dynamic impact: (a) Schematic of FE model; (b) FE model – global view; (c) FE model – close-up view.

2.1.2. Modelling challenges

When performing the contact/impact-related analyses, all contact forces have to be distributed over a priori unknown contact area. Also, the distribution of contact forces is another primary unknown to be determined. These unknowns bring about many FE modelling difficulties. In this section, both the difficulties for the general FE-based contact/impact models and the specific W/C model are discussed.

(a). General modelling difficulties

(1) Unwelcome "gaps and/or penetrations": Small geometrical "gaps and/or penetrations" between the contact bodies are easy-induced and 'unavoidable' at the start of the contact modelling, because of the unknown first point of contact, the misaligned contact positions, the numerical round-off [43], etc. If these "gaps and/or penetrations" are not treated appropriately, they can proactively trigger the problem of divergence in the implicit FE analyses as well as the undesired failure of the explicit FE analyses [35];

(2) Lack of targeted mesh refinement: Usually, the undeformed contact bodies are discretized and further refined at the vicinity of the potential contact areas according to the analysers' experience or visualisation [39]. Thus, the sizes of these areas can be easily overestimated or underestimated, which will lead to either prohibitive computational expense or inaccurate contact solutions. Considering that the desired mesh size within the potential contact area (no less than 1.3mm to ensure the engineering accuracy according to [36]) is 1000 times smaller than the typical dimension of the wheel and rail components (usually in the meter-scale), an economic (efficiency), adaptive (flexibility) and reliable (reliability) mesh refinement has always been a strong challenge for researchers and engineers;

(3) Demand for effective mesh transition: The surface-based tie constraints (similar as bonded contact, constraint equations, etc.[43]), which can bond together two regions having dissimilar mesh patterns (See Figure 4b-c), are commonly used in the contact/impact FE models. As the tie constraints might adversely affect the overall integrity/stiffness of the contact bodies and thus the accuracy of FE simulations [39], the applicability of tie constraints is doubted if they are used without careful examinations.

(b). Specific modelling difficulties

Regarding the W/C model, special FE modelling difficulties (apart from the general ones) will be encountered. These special challenges are mainly induced by the varying

contact geometries of the crossing rail, in which two separated running bands shaded with the yellow and diagonal patterns can be observed (See Figure 4a). One of the running bands lies on the wing railhead, while the other one locates on the nose railhead. To have a better insight on the specific modelling difficulties, they are collected and illustrated as follows:

(1) To identify the potential contact areas: The best identified potential contact areas should be slightly larger than the actual ones, which will enable the good compromises between calculation accuracy and efficiency. In order to maintain the compromises and further facilitate FE modelling process, the exact locations of the potential contact areas (e.g., the starting and ending positions, the lateral width of the area, etc., See Figure 4a) are practically necessary.

(2) To accomplish the 'separate' & 'dependent' mesh transitions: Here, 'separate' means that the mesh refinements at the railhead (including both the wing and nose rail) are to perform and function independently in the longitudinal direction (i.e., travelling direction)(See Figure 4a). The meaning of 'dependent' are twofold: a) In the vertical direction, the bonds between the coarse mesh at the rail-bottom (namely, the rail web and rail foot) and the fine mesh at the railhead are to be secured by a group of solid elements (the mesh sizes are in a descending order) instead of the artificial tie constraints (See Figure 4b); b) In the lateral direction, the rail-bottom mesh refinements on the wing and nose rails have to match with each other (See Figure 4c).

In summary, both the wing and nose rails need to be modelled carefully and further discretized properly so as to fully encompass the double points of contact in the transition region. More information of addressing these modelling (i.e., mesh refining) challenges are given in Section 2.2.2.

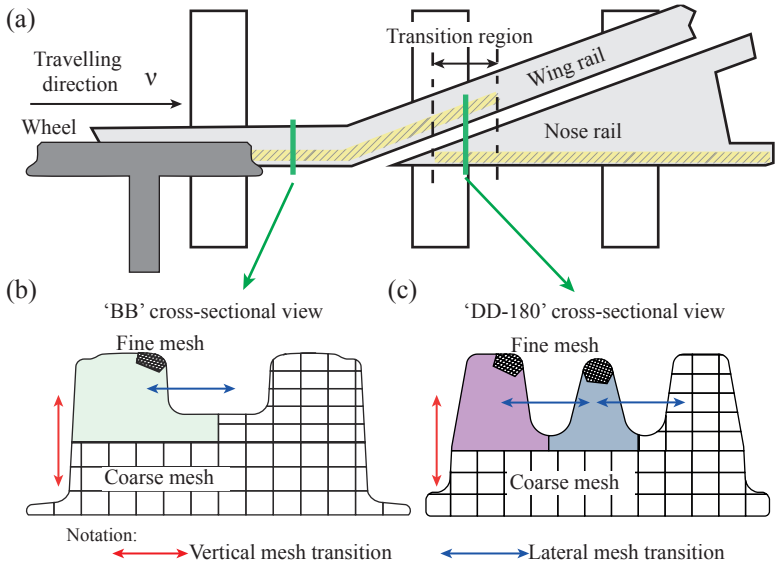

Figure 4: Schematic of mesh refining difficulties: (a) Top view of mesh transition (Notation: regions shaded with yellow colour & diagonal pattern indicate potential contact areas); (b) Mesh transition at 'BB' cross-section; (c) Mesh transition at 'DD-180' cross-section.

2.2. Coupling strategy

To address the aforementioned FE modelling challenges of W/C dynamic impact analysis, a coupling strategy (See Figure 5) that combines the two dimensional geometrical (2D-Geo) contact analyses and 3D-FE analyses, is used.

The basic working mechanism of this strategy is shown in Figure 5. The 2D-Geo simulation is performed first to detect the initial "Just-in-contact" point (CP) and the "Contact clearance" δy. Here, the term "Contact clearance (δy)" is referred to as the vertical distance between the un-deformed contact geometries of wheel and crossing rail (See Figure 7a1-a2). The contact information obtained is used as a helpful guidance to identify the single point and double points of contact, which are then used in the FE mesh refinement. To make this strategy perform well, the data exchange between 2D-Geo and 3D-FE models is accomplished through an external MATLAB routine. Once the 3D-FE modelling and preloading processes are accomplished with the aid of the 2D-Geo model, the implicit-to-explicit sequential FE simulations are performed to analyse the contact behaviour of W/C dynamic impact. The details of the 2D-Geo analyses and the interfacing schemes of the coupling strategy are described in the later sections.

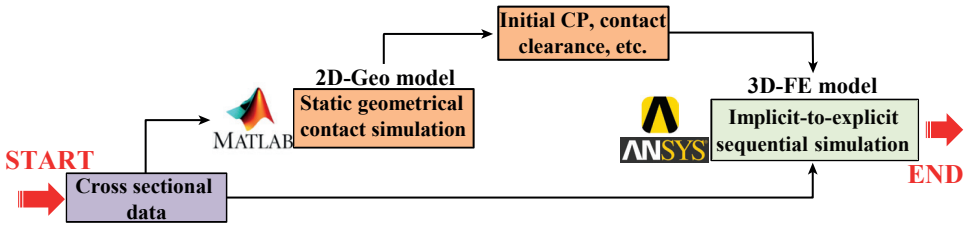

Figure 5: Working mechanism of coupling strategy.

2.2.1. 2D-Geo contact model

To better illustrate the 2D-Geo model, a 3D rigid wheel-set is given and positioned over a 3D solid crossing panel as shown in Figure 6a. The global coordinate system *O-XYZ* is consistent with the one shown in Figure 3.

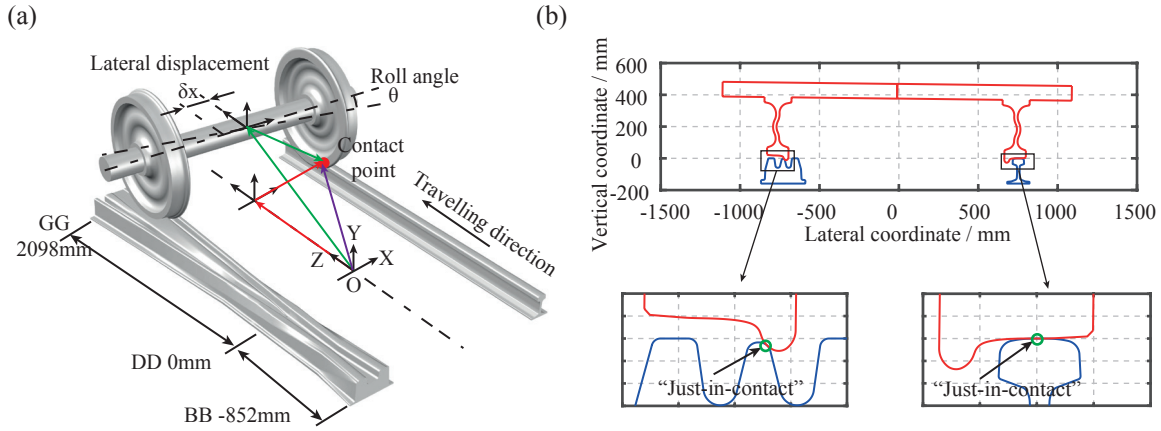

Figure 6: (a) 3D coordinate systems of W/C interaction; (b) "Just-in-contact" equilibrium condition of wheel and DD-180 cross-section at a lateral displacement of -10mm.

The initial contact points, where the two particles on the un-deformed wheel and crossing rail coincide with each other, are determined under given lateral displacements (δx) of the wheel-set. The contact searching procedure is non-iterative (i.e., no 'for/while'

loops used) by taking advantage of efficient matrix operations in MATLAB. Figure 6b shows an example of the 2D-Geo contact analyses, in which the wheel-set is located at the "Just-in-contact" point with a lateral wheel displacement (δx) of -10mm.

2.2.2. Coupled interface & outcome

Based on the 2D-Geo model and 3D-FEM model described above, the interface and outcome of the coupling strategy are presented below.

(a). Refined area identification

Taking the cross-section DD-180 as an example, which is subject to a zero lateral displacement of the wheel-set (See Figure 7a1), the resulting contact clearance is shown in Figure 7a2.

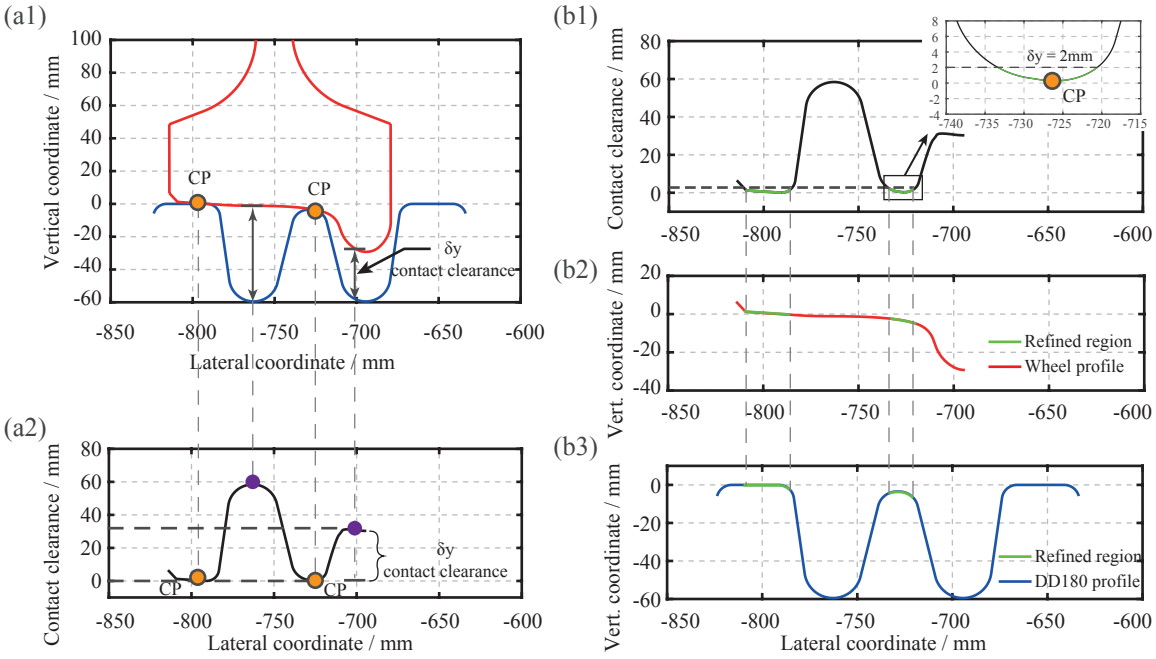

Figure 7: Working procedure of identifying refined potential contact area based on contact clearance: (a1) "Just-in-contact" equilibrium condition of wheel and cross-section DD-180 at a lateral displacement of 0mm; (a2) Variation of contact clearance; (b1) Distribution of contact clearance (0mm$\leq\delta$y$\leq$2mm); (b2) Refined region on wheel profile; (b3) Refined region on rail cross-section DD-180.

Figure 7a1–a2 shows the double point contact, where the value of the contact clearances at the point of contact is almost zero. In order to implement the adaptive mesh refining technique, it is assumed that the most stressed area coincides with the initial contact point (CP). Moreover, the refined region on the contact bodies as indicated by the green highlights (See Figure 7b1–b3), is defined to start from the initial CP and expand to the two ends with a specified contact clearance, e.g. 2mm.

Following the same working procedure as the case of cross-section DD-180, the refined regions of the other characteristic crossing profiles (See Figure 8a) are identified. The varying contact clearances, ranging from 0.5mm to 2.0mm, are prescribed on the basis of local contact geometries. The reason of selecting different contact clearances is to make the size of the potential contact areas wide enough to encompass the actual contact areas, which are strongly influenced by the varying local contact geometries and the amplified impact forces.

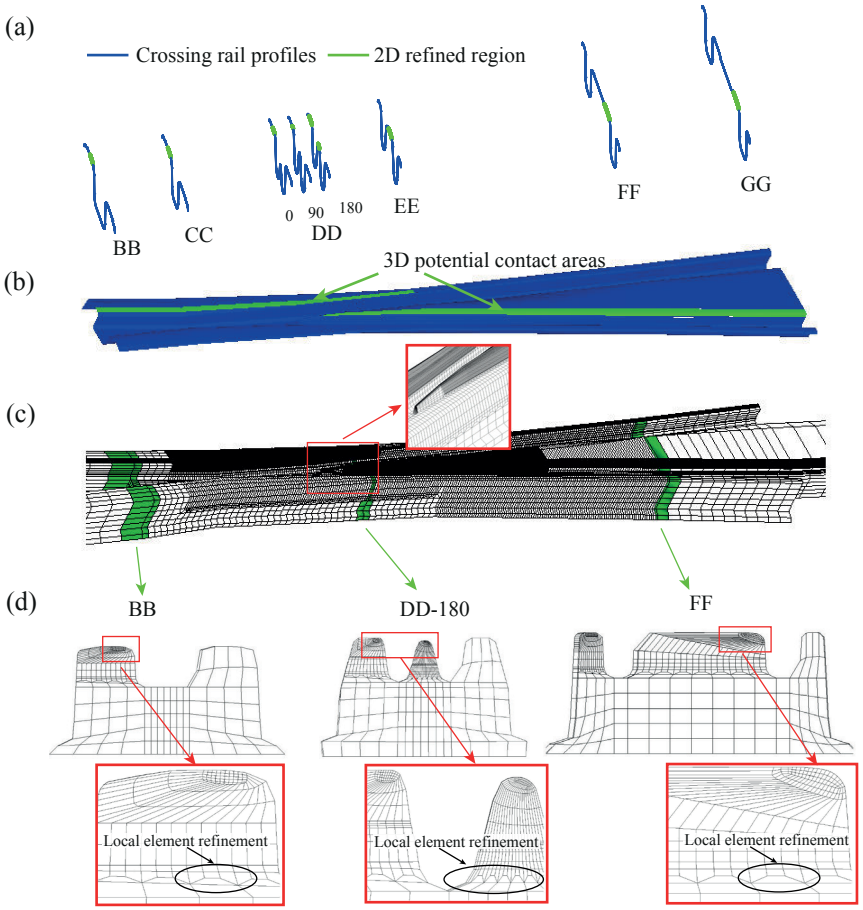

Figure 8: Adaptive mesh refinement on crossing rail: (a) Refined regions of 2D profiles; (b) Refined areas of 3D crossing surface ; (c) Refined 3D FE model; d) Cross-sectional view of refined contact regions.

Figure 8b shows the 3D potential contact areas, which are located on the top of the crossing rail surface. The known relative position between the potential contact area and the crossing rail surface will lead to several separated solid volumes, which are further discretized by sweeping the mesh from adjacent areas through the volume as shown in Figure 8c. Figure 8d shows the cross-sectional view of the refined contact regions.

Regarding the mesh refinement on the wheel, it can be observed from Figure 9a that the regions on the 2D wheel profiles are varying correspondingly from the field side to the flange root, when the wheel is travelling from the characteristic cross-section BB to GG. Using the present FE modelling and meshing techniques, it is still challenging to generate a flexible 3D mesh refinement along the circumferential path of the wheel according to the varying refined regions. Thus, it is simplified into a uniform mesh, starting from the field side and ending up to the flange root as shown in Figure 9b. By this means, the wheel FE model (See Figure 9c) is capable of encompassing all the green highlighted potential contact areas.

Moreover, Figure 8d and Figure 9b show that the difficulties of transitions between the coarse and fine mesh patterns are addressed successfully. The coarse elements are split into three fine elements smoothly using the technique of "Local element refinement" [43].

(b). Resulting contact pair

For the explicit FE simulations (ANSYS LS-DYNA), a pair of contact segments,

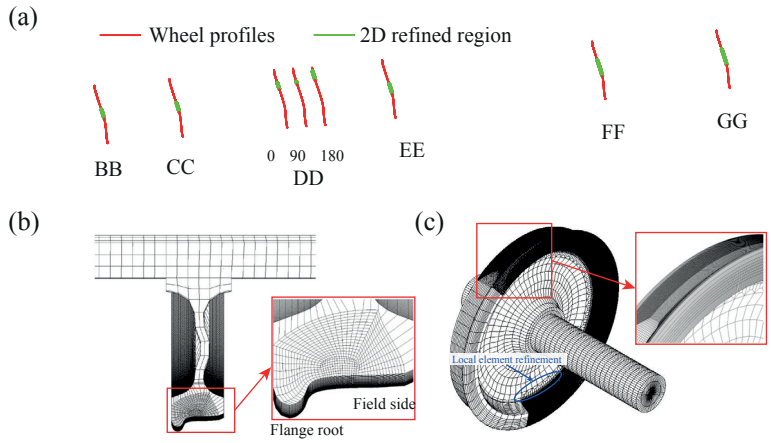

Figure 9: Adaptive mesh refinement on the wheel: (a) Refined regions of 2D wheel profiles; (b) Cross-sectional view of wheel mesh refinement; (c) Wheel mesh refinement along circumferential path.

namely, master and slave segments for explicit FE analysis (target 170 and contact 173 elements for implicit FE analysis, See Figure 10), are required to track the kinematics of the deformation process. Here, the contact segments are the components of nodes on the outmost surface layer of the W/C contact bodies. The penalty method [42] is used to enforce the contact constrains, where a list of invisible "interface spring" elements are placed between all the penetrating slave segments and the master segments. Friction in LS-DYNA is based on the Coulomb formulation [42]. More information about the contact algorithms can be found in [38, 42].

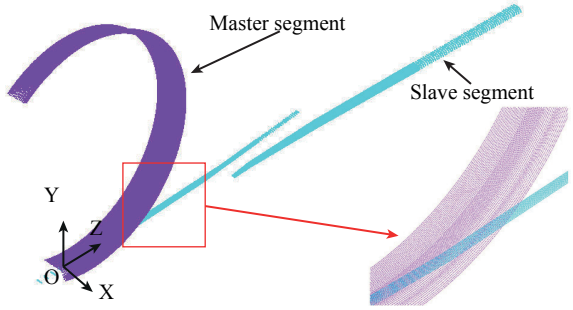

Figure 10: Isometric view of contact pair.

2.3. Effectiveness of 'eFE-CS' model

In this section, the effectiveness of this 'eFE-CS' modelling approach is to be investigated. A comparative study on the performance of the two modelling approaches (i.e., 'eFE-CS' and 'conventional' model, See Figure 11a-b) is performed. The results of this comparative study are presented and discussed.

2.3.1. Setup of comparative study

In the 'conventional' model (used as a reference case), the size of refined regions are selected in another way in comparison to the 'eFE-CS' model. Figure 11b shows that considerably large areas of contact surfaces are refined. Also, the advanced technique of 'local element refinement' is not used. The 3D FE models are generated through simple extruding and/or rotating operations on the 2D meshed cross-sectional areas. Such a

conventional mesh refining technique is easy to implement and often used in the literature. The major difference between the 'eFE-CS' and conventional models lies in their performances (i.e., calculation efficiency, accuracy, flexibility of mesh refinement, etc.), which are discussed in Section 2.3.2.

Both the same crossing rails (1:9–54E1) and the same wheel profiles (S1002) are used in the two models. Also, the same material properties of track components listed in Table 1 are adopted. The wheels are prescribed to run over the same rolling distance of 1.2m. The mesh sizes on the wheel and rail interface in the vicinity of the potential contact area are all limited to 1.0mm.

The simulations are performed on a workstation with an Intel(R) Xeon(R) @ 3.10 GHz 16 cores CPU and 32GB RAM. The shared memory parallel processing capability of ANSYS LS-DYNA is used. For each simulation, 8 parallel licenses are employed in order to shorten the elapsed time necessary to run an analysis. The model-solving power is distributed over multiple processors on the same workstation. Such a setup of comparative study is to ensure that both models work in the same operational conditions.

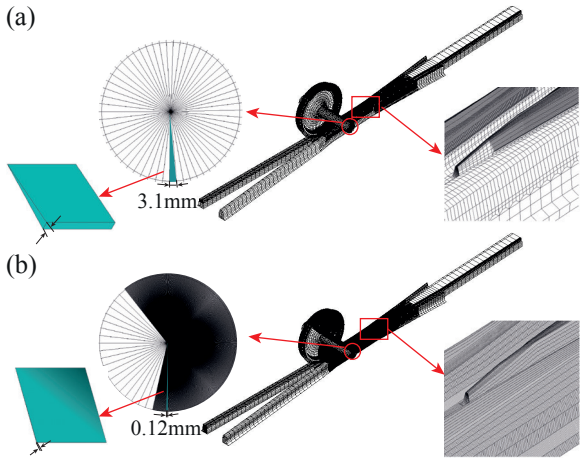

Figure 11: Comparison of FE models: (a) 'eFE-CS' model; (b) Conventional model (reference case).

2.3.2. Comparison of FE models

Under the same modelling and/or operational conditions, the quantitative results of the two models are listed in Table 2. It can be seen that the number of elements of 'eFE-CS' model is only 1,108,285, while the 'conventional' model has an increases of 33.8%. In the 'conventional' model, many warning/poor elements are induced by the mesh concentration at the wheel axle centre due to the rotating mesh operations (See Figure 11b). The amount of the poor elements are 12.62% more than that of 'eFE-CS' model. The minimum side length of the poor elements in the 'conventional' model is 0.12mm, which makes the calculation time step size Δt_{calc} to be as small as 2.45e-9 second. It should be noted that the calculation time step size Δt_{calc} in ANSYS LS-DYNA is determined according to the minimum side length of the elements [42]. Such a calculation time step size Δt_{calc} is 5.93 times smaller than that of the 'eFE-CS' model. Consequently, the small calculation time step Δt_{calc} of the 'conventional' modelling approach manifests itself in the resulting prohibitive calculation expense T_{calc}(1128 hours), which is almost 16.63 times higher than that of 'eFE-CS' model (only 64 hours).

.

Table 2: Comparison of FE models.

Models	Number of elements	Warning/error elements	Δt_{calc} [a] (/second)	T_{calc} [b] (/hour)
'eFE-CS'	1,108,285	4.73%	1.7e-8	64
'Conventional' (reference case)	1,673,507	17.35%	2.45e-9	1128
Relative difference (w.r.t. 'conventional')	**-33.8%**	**-12.62%**	**5.93**	**-94.3%**

[a]: Calculation time step size; [b]: Calculation expense;

2.3.3. Comparison of impact responses

Figure 12a-b show the vertical and longitudinal contact forces obtained from the FE simulations of the two models presented above. These dynamic contact forces are plotted versus the wheel travelling distance. It can be seen that the vertical contact forces vary around the applied axle load (100kN) and hold constant on the straight path (around 100mm long from the starting point of the wheel motion). After that, a noticeable force oscillation is observed. The reason of this force oscillation can be attributed to the geometrical change of the wing rail, which starts to diverge from a straight path to an inclined path (See Figure 12c). For the wheels of conical/worn treads, this causes vertical, downward movements of the wheels, which subsequently induce the oscillations of the contact forces. Taking the wheel contact position at CC cross-section (denoted by a green line) as a reference, it can be clearly seen that the wheel starts to dip downward gradually with a couple of centimetres as it runs further on the inclined wing rail. The downward movement of the wheel (See Figure 12c-d, according to the 2D-Geo contact analyses) leads to the oscillations of contact forces. It is shown in Figure 12a-b that the amplitudes of these contact forces are reducing within the next metre, which are mainly caused by energy dissipation in the vertical damping elements of the wheel and the crossings bedding [12].

As the wheel gets into the location of 180mm away from the nose point, it can be observed from Figure 12c-e that the wheel dips downward into its maximum (1.782mm). After that, the wheel starts to climb upward onto the nose rail, where the sudden strike of the wheel on the crossing rail occurs. The dynamic impact force (around 216kN) is amplified to almost 2.2 times larger than the applied wheel load (100kN). It can be noticed that the change of the dynamic forces agrees reasonably well with the change of the vertical wheel movement. In other words, the wheel 'sink-lift' movement [8] implies the dynamic force oscillations. Such dynamic impact phenomena observed agree reasonably well with the results presented in [12, 24], where it find more that both the wheel dip depth and angle can strongly influence the impact event.

It can also be seen from Figure 12a-b that the variation of the dynamic contact forces obtained from the two simulations are similar to each other. The impact events manifest themselves with a peak value on contact forces at the same location. The value of the maximum impact forces obtained is 216.3 and 195.9kN respectively (See Table 3). The maximum impact force estimated by 'eFE-CS' model is 10.4% higher than that of 'conventional' FE model.

Figure 13 shows the distribution of Von-Mises stress at the location, where the maximum impact force occurs. It can be seen that the contact patch firstly runs only on the wing rail and then it starts to shift onto the nose rail. Two discontinued residual stress areas are left on both the wing and nose rails, which implies the on-site running

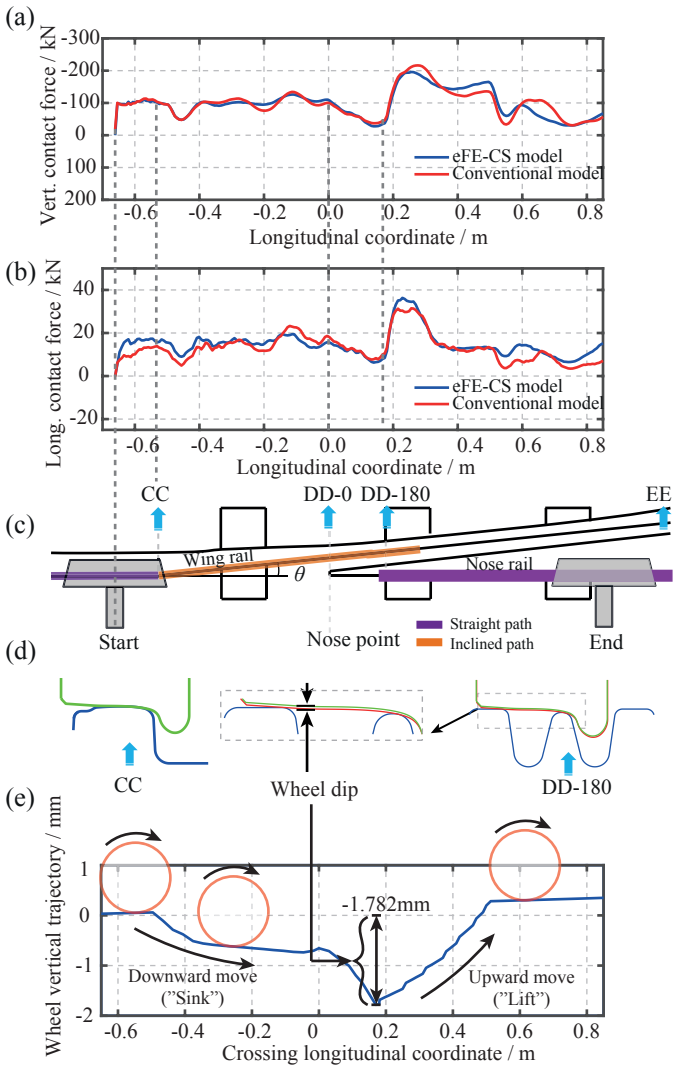

Figure 12: Comparison of contact forces: (a) Variation of vertical contact force w.r.t rolling distances; (b) Variation of longitudinal contact force w.r.t rolling distances; (c) Schematic of W/C interaction; (d) Close-up view of 'wheel-dip'; (e) Vertical wheel trajectory determined by 2D-Geo contact analyses.

bands (more discussion in Section 3.1). Also, the distribution of the Von-Mises stress obtained using the two modelling approaches shows similar pattern. The maximum value of the Von-Mises stress is 1199 and 1044MPa, respectively. The relative difference of the maximum Von-Mises stress is 14.8% (See Table 3).

These differences shown in the results might be attributed to two factors:

- Different calculation time step sizes (See Table 2): For the transient dynamic analyses, it is widely recognised [43] that the accuracy of solution depends on the calculation time step: the smaller the time step, the higher the accuracy. From this point of view, the accuracy of FE results obtained from the 'conventional' model ($\Delta t_{calc} = 2.45e{-}9$) should be higher than that of 'eFE-CS' model ($\Delta t_{calc} = 1.7e{-}8$). However, it is not always the case to have the small time step size, since exceedingly small time step size (e.g., that of 'conventional' model) wastes valuable computer resources and causes numerical difficulties. Moreover, it is worth noting that the accuracy of the results would not increase any more with decreasing time step sizes, if the time step size is sufficiently small.

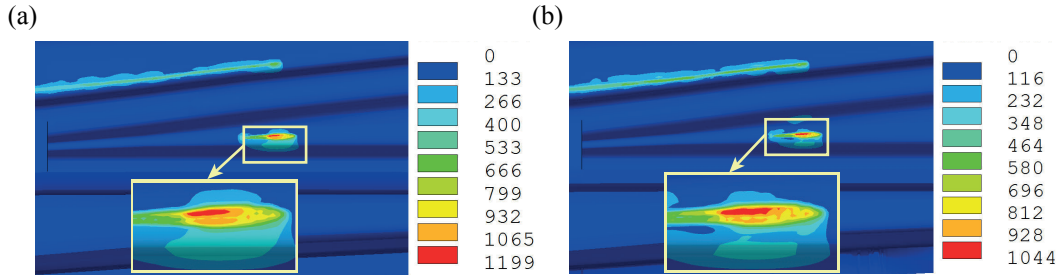

Figure 13: Comparison of Von-Mises stress (Unit: MPa) at most 'impact' moment: (a) 'eFE-CS' model; (b) Conventional model.

- Presence of poor-quality elements (due to the effect of mesh discretization, See Figure 11): The element shape checking (See Table 2) shows that the 'conventional' model has a much bigger (17.35%) population of poor/warning elements than the 'eFE-CS' model (only 4.73%). The presence of those "badly shaped" elements might adversely affect the accuracy of FE simulations and thus cause the discrepancies in the results.

Considering the prohibitive calculation expense of 'conventional' modelling approach (due to the exceedingly small time step size, See Table 2), it can be summarised that the 'eFE-CS' modelling approach performs better than the 'conventional' one.

.

Table 3: Comparison of impact responses from two models.

Models	F_{impact}^{max} [a]/ kN	σ_{vms}^{max} [b]/ MPa
'eFE-CS'	216.3	1199
'Conventional' (reference case)	195.9	1044
Relative difference (w.r.t. 'conventional')	**10.4%**	**14.8%**

[a]: Maximum impact forces; [b]: Maximum Von-Mises stress;

2.4. Discussion: Pros of 'eFE-CS' model

The two computational models/programmes (namely, 2D-Geo contact model and 3D FE model), which are often used separately to fulfil different engineering purposes, are seamlessly coupled together. The presented coupling strategy does not simply refer to the two programmes themselves, but more means the data exchange and interfacing mechanism between them. The effectiveness of the developed 'eFE-CS' model has been demonstrated through a comparative study. Based on the outcome of those coupling operations and the FE simulation results, the advantages of this coupling strategy are summarised as follows:

- General modelling challenges (See Section 2.1.2): The unwelcome "Gaps/Penetrations" at the beginning of the W/C contact modelling have been significantly reduced into a tolerable level by positioning the wheel exactly onto the "Just-in-contact" point of the crossing rail. It can be learned that the 'eFE-CS' strategy can work not only well for the cases of wheel-rail interaction [35, 38, 39] but also effectively for the analyses of dynamic impact between wheel and crossing.

- Specific modelling difficulties (See Section 2.1.2): Using this coupling strategy, the two 'separate' potential contact areas on both the wing and nose rails are identified and refined properly. Also, the "Local element refinement" enables the smooth transitions between the bonds of coarse and fine mesh in both the lateral and vertical directions.

- Improved calculation efficiency: The number of FE elements in the 'eFE-CS' model has been significantly reduced in comparison with that of the 'conventional' model, which can greatly save the memory space. The minimum side length of the elements has been increased a lot, which will maintain a relatively large calculation time step. Thus, the calculation efficiency has been significantly improved.

- Good calculation accuracy: The deviations of FE simulation results obtained from the two models are relatively small. It implies that the 'eFE-CS' model can produce as accurate results as the 'conventional' FE model. Also, the amount of the poor/warning elements is reduced and the elements having good quality are guaranteed.

To sum up, the 'eFE-CS' modelling approach with application to the analysis of dynamic impact in a 1:9 railway crossing panel is quite effective. The proposed coupling strategy is a nice assistant in advancing the FE modelling of W/C dynamic impact. Also, the 'eFE-CS' strategy is not limited to contact modelling in the railway community, but also recommended to use in other mechanical contact/impact systems having complex local contact geometries (e.g., gear, worn bearing, etc.). The limitations/cons of the present 'eFE-CS' model and its further improvement are discussed later in Section 4.3.2.

3. Experimental validations

In this section, the transition regions (Definition, See Section 1) estimated by the 'eFE-CS' simulations are compared firstly with the field measured ones, which are further extended from the authors' former work [3]. Furthermore, the crossing accelerations determined by the FE simulations are compared with the measured ones using the on-site acceleration measurement device.

3.1. Model validation via transition regions

To evaluate the accuracy of the transition region predicted by the 'eFE-CS' model, the transition regions measured from the field are collected and compared. Also, the transition region estimated by the 2D-Geo contact analyses is used for comparison.

3.1.1. Field measured transition regions

Figure 14a-b show the measured transition regions at the field. It can be seen from Figure 14a that the transition process starts at 180mm away from the nose point and ends at 300mm. The overall length of the transition region (also called transition distance) is approximately 120mm. After more than one year's service, the start point of the transition region shifts around 20mm towards the nose point, while the end point moves 20mm away from its original location. The resulting transition distance expands to 160mm long. It should be noted that during the period between measurement 1 and 2, there are several operations of welding and grinding performed to eliminate the surface defects (e.g., the one shown in Figure 1d) on the crossing rail.

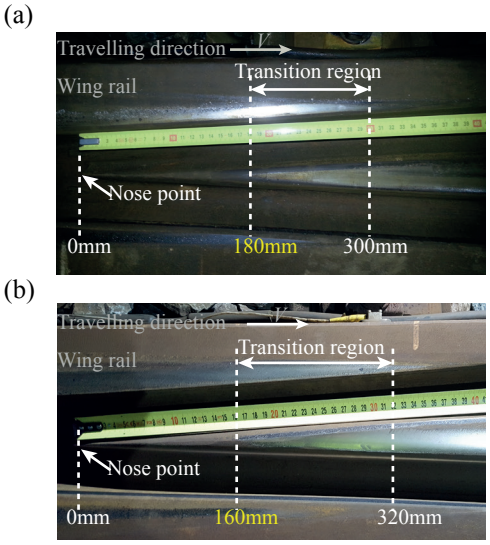

Figure 14: Field measured transition regions (photos taken by Y. Ma): (a) Measurement 1 (14/December/2015); (b) Measurement 2 (around one year later, 06/February/2017).

3.1.2. FE simulated transition region

To predict the transition region, the areas of residual Von-Mises (also called 'equivalent/effective') stress/strain are suggested to use as an indicator. Here, the term of 'residual' is referred to as the stresses/strains that are locked/frozen in the W/C contact bodies after the original cause of contact stresses has been removed (i.e., the wheel has rolled over the crossing rail).

The choice of Von-Mises stress/strain (as opposed to many other potential important stress/strain measures) is based on the complexity of contact loadings, which are multiaxial (i.e., mix of large normal and shear stresses) and non-proportional. Only one independent component of stresses/strains (e.g., contact pressure, shear stress, etc.) might be insufficient to represent such loading conditions and to ensure the accurate prediction of transition regions.

It should be noted that this suggested area of residual Von-Mises stresses/strains might not always yield the perfect indication of transition regions for all kinds of loading conditions (e.g., at low contact load, no yield or plastic deformation occur but wear still exists). But it suits well to the study of dynamic impact at 1:9 crossing panel, since the resulting stresses substantially exceed the yield strength of the material (See Section 4).

Figure 15 shows the distribution of Von-Mises stress and plastic strain, which are determined by the 'eFE-CS' simulations. The two plots are captured at the same moment. The regions at the far right side of each plot indicate that the wheel is standing on the top of the crossing rail. The remained areas show the distribution of residual stresses/strains.

The transition region begins at approximately 180mm far from the nose point. After 43mm away from the starting point, the transition region ends. The maximum value of the plastic strain is as large as 3.5%, while the maximum residual stress is 825MPa.

3.1.3. 2D-Geo estimated transition region

Figure 16a shows a number of crossing rail profiles, which are located at arbitrary locations along the track. They are generated by longitudinally interpolating the two adjacent characteristic cross-sections (as shown in Figure 2). Based on the interpolated profiles of crossing rail, the transition region can also be predicted using the 2D-Geo contact model (as described in Section 2.2.1).

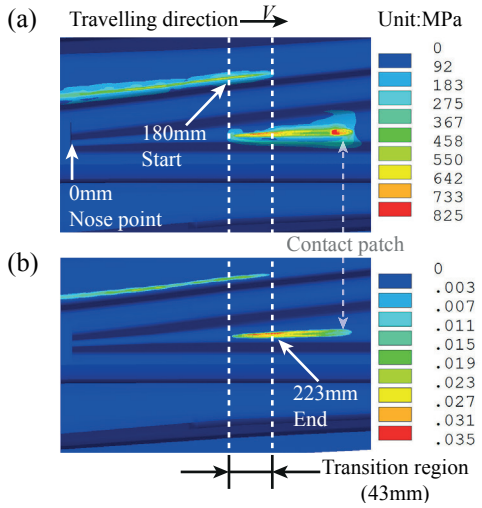

Figure 15: Variation of transition region determined by explicit 3D FE analysis: (a) Von-Misses stress; (b) Von-Mises plastic strain.

Figure 16b shows that the transition region also starts at a point which is 180mm far away from the nose point. The estimated transition distance is as short as 25mm.

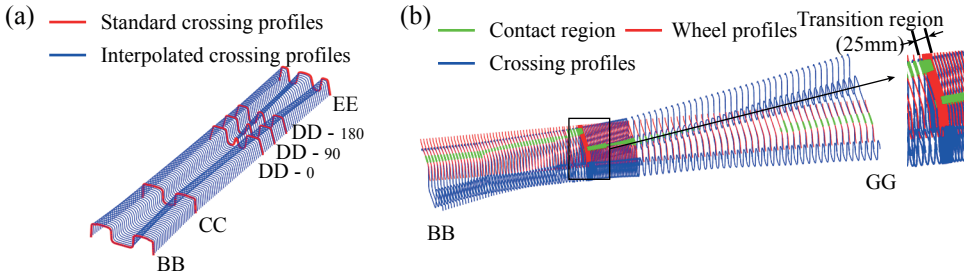

Figure 16: Variation of transtion region determined by 2D-Geo contact analyses: (a) Interpolated cross-section profiles between characteristic cross-sections; (b) Close-up view of transition region.

3.1.4. Comparisons and discussions

Table 4 lists the results of comparison of the transition regions. A good agreement on the estimated start points of the transition region is observed. However, for the end position of the transition region, the FE result deviates much from both the 2D-Geo estimated results and the field measurements. It ends later than the estimation of 2D-Geo analyses, but much earlier than the field measurement.

The discrepancies between the FE-estimated transition region and the corresponding field measured data are explainable, since the present 'eFE-CS' simulations are only focusing on standard and undeformed wheel & crossing rail profiles. Also, no lateral shifts and yaw motions of the wheel are considered in the FE model.

However, in reality, the wheel/crossing rail profiles of different conditions (i.e., degraded, improved/repaired, newly replaced interfaces, etc.) are in use. The relative positions of the wheel-sets vary commonly during the process of W/C dynamic impact. In addition, the field measured transition regions are formed after multiple wheel passages, while the FE prediction only represent one wheel passage. All these uncertainties and/or variabilities can proactively affect the evolvement of the contact patch and further on the transition region.

.

Table 4: Comparison of transition regions.

	Transition region */mm		Transition distance /mm
	Start	End	
'eFE-CS' simulation	180	223	43
Measurement 1	180	300	120
Measurement 2	160	320	160
2D-Geo estimation	180	205	25

*: 0mm is referred to as the nose point.

With respect to the prediction of 2D-Geo contact analyses, the discrepancies to the FE-estimated transition region are small but still distinguishable. In the 2D-Geo contact analyses, two contact bodies are assumed to be rigid (i.e., no elastic and/or plastic deformations). The double point contact, which indicates the transition region, is determined on the basis of the prescribed tolerance (i.e., as small as 0.1mm). Regarding the 3D-FE contact analysis, the elastic-to-plastic material behaviour is considered. Also, the transition region is indicated by the area of residual stress. Such differences explain the discrepancies observed.

The comparative study shows that the FE-predicted transition region is in good correlation with that of measurement. It demonstrates that the proposed 'eFE-CS' model is capable of simulating the W/C dynamic impact accurately.

3.2. Model validation via crossing accelerations

In this section, a general introduction of the acceleration measurement device is given first. Following that, a detailed comparison between the field measured and FE simulated accelerations is made.

3.2.1. Measurement device: ESAH-M

Figure 17 shows the general working scheme of the measurement device ESAH-M (Elektronische System Analyse Herzstijckbereich – Mobil) in the field. Basically, there are four main components involved [4, 44]:

(1) Two inductive sensors (called 'BERO'): to detect the number of running wheel axles and determine the associated train velocities;
(2) One magnetic triaxial acceleration sensor: to measure the accelerations of the crossing rail in three dimensions;
(3) One sleeper displacement sensor (Optional): to record the vertical displacements of a sleeper optionally;
(4) One main battery powered unit: to process (i.e., receive, synchronise, save and transit) all the acquired field data (including the train velocities, sleeper displacements, crossing accelerations, etc.).

The measurement range of the accelerometer is 500g. The sampling frequency of acceleration measurement device is 10kHz. To make a reasonable comparison of the FE acceleration signal with the measured acceleration signals (400 axle of 21 trains), only the cases of regular contact are studied. The remaining cases of irregular contact are excluded from current comparison, since the present FE model focuses on the cases of regular contact. The statuses of regular and irregular contact (See more information in

[4, 5, 44]) are detected according to the direction and the magnitude of the measured accelerations.

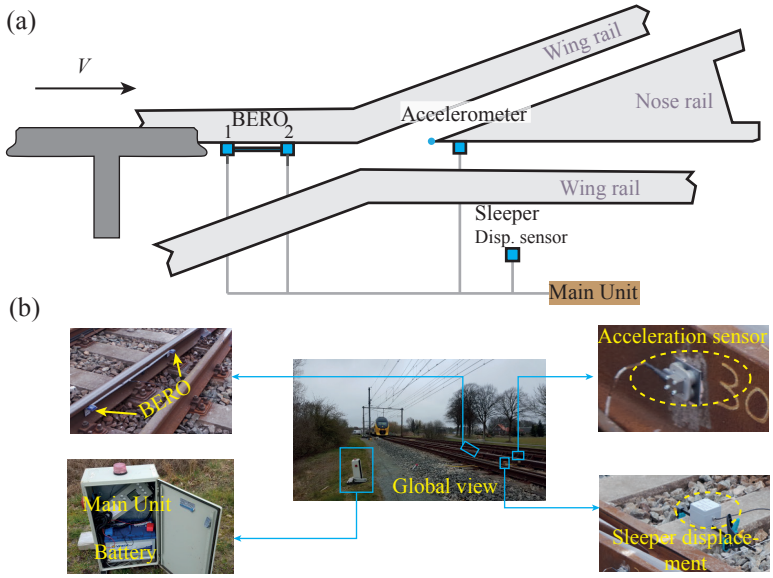

Figure 17: (a) Schematic of ESAH-M acceleration measurement; (b) Global and close-up views of ESAH-M measuring device at the field (photos taken by V. Markine, the one of 'global view' is shared by X. Liu).

3.2.2. FE simulated acceleration

Figure 18 shows an example of FE simulated crossing acceleration. The FE-based accelerations are extracted from a group of selected nodes (See Figure 18a), which are located at the same position as the acceleration sensor of ESAH-M (See Figure 18b). This ensures the comparability of acceleration sources.

To accurately describe the FE acceleration signal, 2000 sampling time points are selected. The resulting sampling frequency, which is the ratio between the number of the sampling points (2000) and the calculation time (0.044s), is around 45kHz. The maximum acceleration amplitude is around 38g.

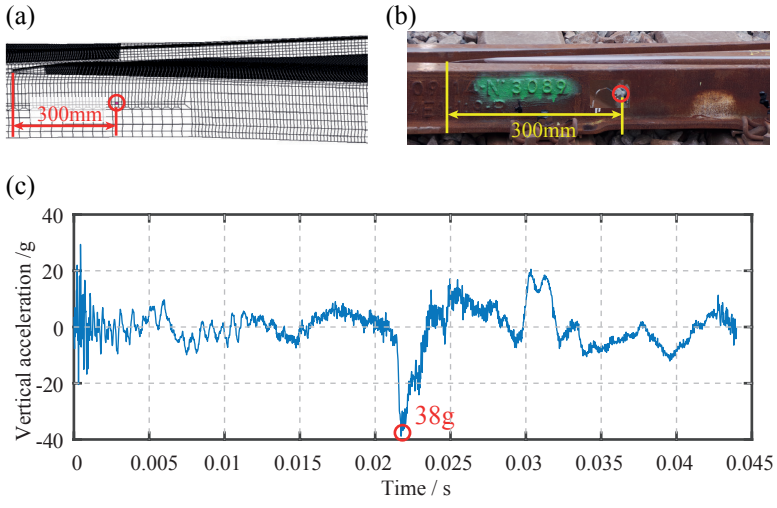

Figure 18: Example of FE simulated acceleration: (a) Nodes to extract FE simulated accelerations; (b) Location of acceleration sensor at the field; (c) FE simulated vertical acceleration.

3.2.3. Results of comparison

Figure 19 shows the comparison of the FE simulated accelerations with those measured from the field. The measured accelerations of more than 85% axles (169 out of 197), which are in regular contact, are plotted in grey. The reason of not using all the measured acceleration signals of regular contact is to exclude the faulty signals [44], which are automatically detected by the ESAH-M programme itself. The measured mean acceleration is plotted in green. It can be seen that the variations of both the measured and FE simulated accelerations follow the "V" pattern. Such a "V" pattern is in good relation with the 'sink-lift' movement of the wheel vertical trajectory (See Figure 12e) as well as the oscillation of vertical contact forces (See Figure 12a).

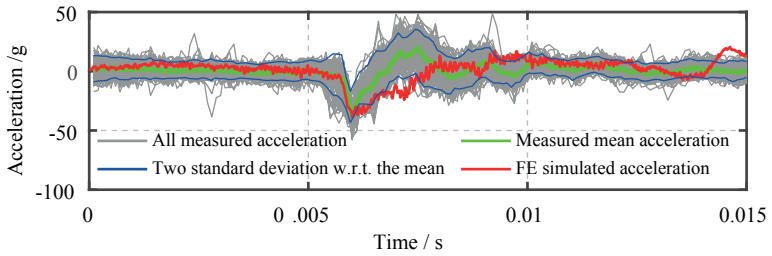

Figure 19: Comparison of FE simulated acceleration with measured ones in time domain.

Figure 20a shows the results of the statistical analysis on the maximum amplitudes of the measured accelerations. The number of the occurrences of maximum accelerations is plotted at a interval of 1g (e.g., 20g-21g, 21g-22g, and so on). Ultimately, all these measured accelerations are categorised and visualized by bars in a histogram.

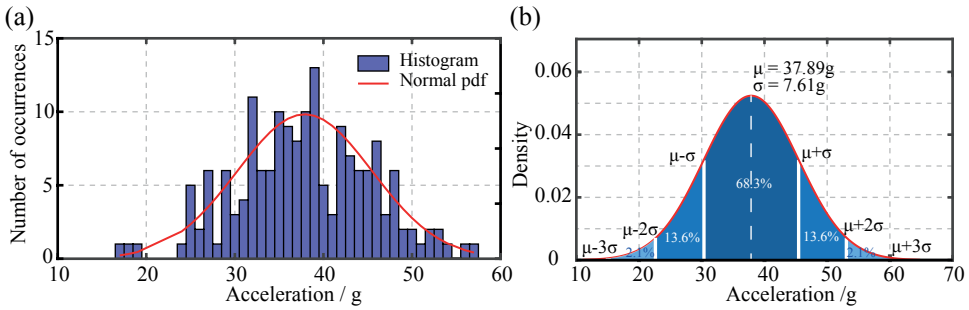

Figure 20: Statistical analysis on maximum amplitudes of measured accelerations: (a) Histogram; (b) Normal distribution.

The resulting histogram has a normal distribution (bell-shape) as shown in Figure 20a-b. The mean μ of this normal distribution is 37.89g, while the standard deviation σ is 7.61g. In Figure 20b, the area of dark blue-grey implies one standard deviation from the mean, which accounts for 68.3% of this sampling population. The area of two standard deviations with respect to the mean accounts for 95.5%. Figure 19 shows the measured mean and a band representing two standard deviations from the mean. It can be noticed that the magnitude of the FE simulated acceleration (38g, See Figure 18c) exactly falls within the range of the two standard deviation from the measured mean. To summarize, the FE simulated acceleration agrees reasonably well with the ones from acceleration measurements.

3.2.4. Discussion: Source of discrepancies

The sources of these discrepancies might be categorised into three groups, namely the different operational patterns, track parameters and FE model capability:

(1) Operational patterns: The FE simulation is performed with a nominal operational pattern (i.e., train speed, axle load, traction, etc.), in which these operational parameters are prescribed to determined values as shown in Table 1. In reality, the operational patterns are uncertain. The parameters such as, train speeds, axle loads, traction forces, wheel profiles,etc. strongly depends on the type/condition of vehicles. The difference of operational patterns might change the distribution of transition regions and cause the variation of accelerations.

(2) Track parameters: The degradation and/or maintenance (i.e., grinding, welding, etc.) of W/C interfaces will change the local contact geometries. The components of substructure will degrade (e.g., sleeper, ballast settlement, gaps between sleepers and ballast, etc.) and have to be maintained in time. The variation of track properties (i.e., mass, stiffness, damping, etc.) will lead to the distinguishable discrepancies.

(3) FE model capability: The present FE model is capable of simulating the single wheel-crossing interaction. But it is still far from the real case of complete vehicle-track interaction. As a result, the influence of the second wheel (i.e., the one on the stock rail) and bogies on the impact phenomenon might not be fully considered.

Although the tolerable deviations of the impact signals exist, the FE simulations results agree reasonably well with ESAH-M measurements. It also implies that the FE model is quite promising to be used to simulate the W/C dynamic impact.

4. FE simulation results and discussions

Using the validated FE model, a series of FE simulations are performed. In this section, the FE results including both the surface and subsurface contact properties are presented. These contact properties are usually captured at a relatively large number (e.g., 2000) of time points all through the explicit FE simulation. Here, the term 'time points' relates to the variation of contact locations along the crossing rail. Figure 21 shows the variation of contact forces with respect to different time points (i.e., the equivalent of different contact locations). It can be seen that only the contact properties at the specified time points ranging from "A" to "H" are extracted, since the corresponding impacts are most significant at the vicinity of the transition region.

4.1. Surface stress response

As mentioned above, the surface contact properties are only extracted at the specified time points shown in Figure 21. The distribution of normal pressure, shear stress, slip-adhesion areas, etc., is presented.

4.1.1. Normal pressure

The contact patches from the FE analyses are determined according to the normal contact pressure [36]:

$$A\ node\ is\ in\ contact\ if: \sigma_n > 0 \tag{1}$$

where σ_n is the nodal pressure in the direction normal to the local contact surface. Figure 22 shows the contour plots of the normal pressure distribution at the selected time

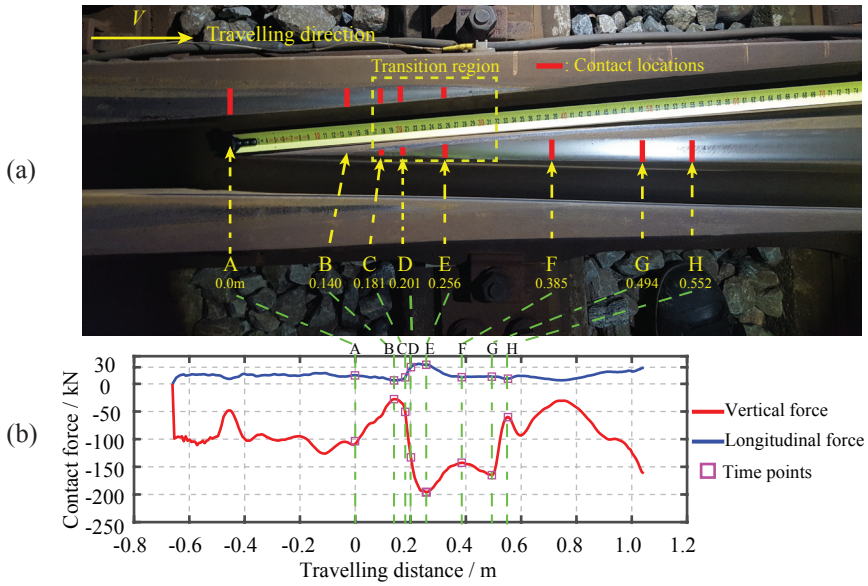

Figure 21: Schematic of time points (i.e., contact locations ranging from 'A–H') to extract contact properties: (a) Corresponding contact locations on crossing rail; (b) Variation of contact forces at specific time points.

points. In order to better demonstrate the distribution of surface contact pressure, the compressive pressure is treated as positive. It can be seen that all the resulting contact patches are non-elliptical. Also, at the time points of "C" and "D", double contact patches are observed, which manifest themselves in practice as the collateral running bands on both the wing and nose rails.

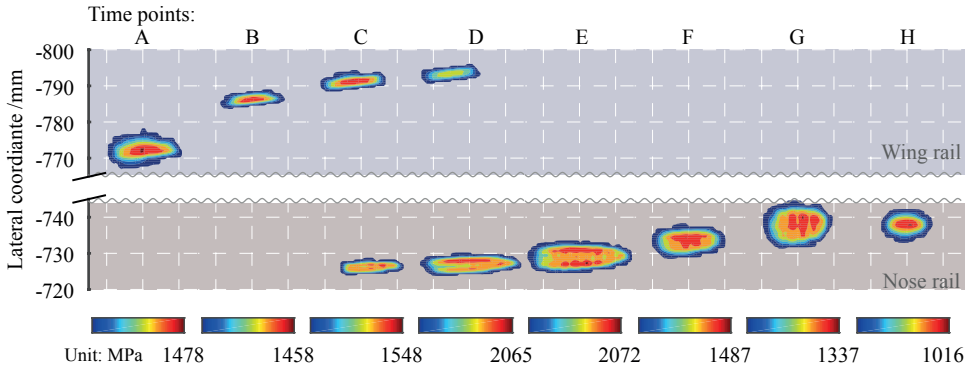

Figure 22: Surface normal pressure distribution.

Table 5 lists the results of the normal pressure and the contact patches. The maximum normal pressure obtained at the time point "E" amounts to 2072MPa. That is 96.4% higher than the one in the case of normal wheel-rail interaction [38].

Under such a high impact loading condition, it is found that the relative difference of the contact area between the solutions of normal wheel-rail and wheel-crossing interaction is also big (See Table 5 -74.7% in the time point "B" and 16.4% in the time point "D"). This clearly shows the effect of varying crossing geometry on the contact properties.

4.1.2. Shear stress

Once the normal contact is established, the imposed driving (or braking) torque leads to the relative difference between the rolling velocity and longitudinal velocity. Accord-

Table 5: Comparison of the contact solutions at different time points.

	W/C impact at different time points								Normal W/R interaction [38]
	A	B	C	D	E	F	G	H	
Contact status [a]	1	1	2	2	1	1	1	1	1
σ_n^{max} / MPa [b]	1478	1458	1548	2065	2072	1487	1337	1016	1055
τ^{max} / MPa [c]	326	423	460	542	451	279	262	278	260
A_c / mm^2 [d]	156.2	64.8	154.3	298.5	215.2	154.8	202.0	105.0	256.5

[a]: Number of contact patches; [b]: Maximum normal pressure; [c]: Maximum shear stress; [d]: Area of contact patch.

ingly, the wheel exhibits a slip in the direction opposite (or parallel if braking) to the travel of vehicle. The friction in the tangential direction builds up to resist the relative motion between two contact bodies.

Depending on the magnitude of the applied traction (i.e., driving torque), the statuses of contact can be classified into partial slip (or slip-adhesion) and full slip (sliding). In the state of partial slip, the applied traction is smaller than the frictional force. With the increase of the applied traction, the slip region spreads forwards from the leading edge of the contact patch until the slip zone reaches the leading edge and full slip occurs [46]. At the point of transition from partial slip to full slip, the traction is equal to the frictional force. In general, the traction is limited by the friction and is sometimes called the utilized friction [45]. To focus the attention on the partial slip contact(i.e., commonly occur in the process of wheel-rail interaction), the coefficient of friction is assumed to be 0.5 and the coefficient of traction is 0.25. The value of these two operational parameters is adapted from [18, 36], where the maximum tractive effort of the locomotives is considered. Note that the model can easily be adjusted for other operational parameters (See [38]). More information about the friction coefficient and the applied traction can be found in Table 1.

Figure 23 shows the distribution of shear stress on the surface of crossing rail. These shear stresses are captured at the same moment as the contact pressure. For both cases, the major portion of the shear stress is located at the rear part of the contact patch.

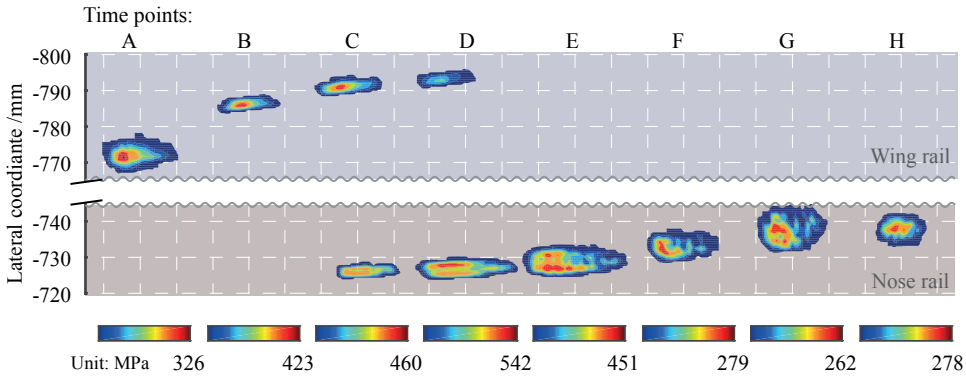

Figure 23: Surface shear stress distribution.

The maximum shear stress is 542MPa (Time point: 'D'), which is 108.5% higher than the one in the case of wheel-rail interaction (260MPa) [38]. These high shear stresses indicate the high risk of surface damages on the crossing rail (See Figure 1).

4.1.3. Slip-adhesion phenomena

Under the condition of partial slip, the contact area is divided into two regions of slip and adhesion [27]. However, the division of contact area is not known in advance and must be found by trial [46]. Following the well-established criterion described in [31, 36],

$$A\ node\ is\ in\ adhesion\ if: \mu|f_{n\_N}| - |f_{n\_T}| > \varepsilon_T \tag{2}$$

the phenomena of slip-adhesion can be explored. Here, f_{n_N} is the nodal normal force, f_{n_T} is the nodal tangential force in the longitudinal direction, and ε_T is the tolerance for distinguishing the slip and adhesive areas. The magnitude of ε_T is prescribed to be the 10% of the maximum traction bound force [38].

It should be noted that the effectiveness of the tolerance suggested has been assessed in the authors' previous work [38], where verifications of varying operational patterns (i.e., applied traction, friction coefficient, etc.) against CONTACT have been performed extensively. The results show that such a tolerance fits well to the case of FE-based W/R contact analysis under the consideration of realistic profiles.

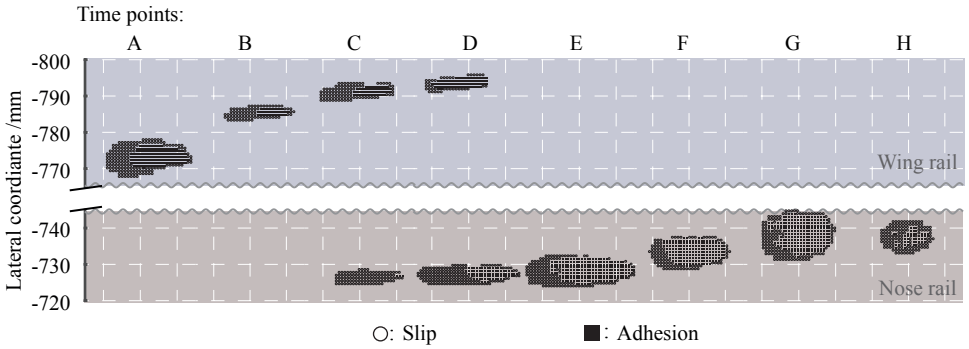

Figure 24: Slip-adhesion area plot.

Figure 24 shows the distribution of slip-adhesion area according to Equation 2. As it can be observed, the leading areas of all the contact patches are in adhesion, whereas the trailing areas are in slip. Such an observation conforms well with the classical frictional rolling contact theories [27, 46].The relationship between the obtained contact properties and surface degradation will be discussed later in Section 4.3.1.

4.2. Subsurface stress response

To check the stress responses on the sub-surface, two orthogonal sliced planes, namely "AA" and "BB", are introduced as shown in Figure 25b & Figure 26b. "AA" is sliced at the initial contact point along a longitudinal-vertical plane, while "BB" is located at the same point but along a lateral-vertical plane. The stresses mapped on the two cutting surfaces are presented in this section.

4.2.1. Von-Mises stress

Generally, Von-Mises stress is adopted as a measure of material performance assessment under specific contact conditions for elastic-plastic material. Thus, the most critical moment, when the Von-Mises stress reaches peak value (Time point: 'E') at a distance of 223 mm away from the crossing nose point, is examined as shown in Figure 25a-b.

It can be seen that the maximum Von-Mises stress of 1197MPa is far above the yield limit (480MPa) of the materials. Such a high stress concentration is attributed to the relatively small size of the contact patch as well as the amplified impact loads. Figure 25c-d show that the maximum Von-Mises stress is concentrated at a small volume of material, which is ranging from the rail top surface to 2.0mm beneath.

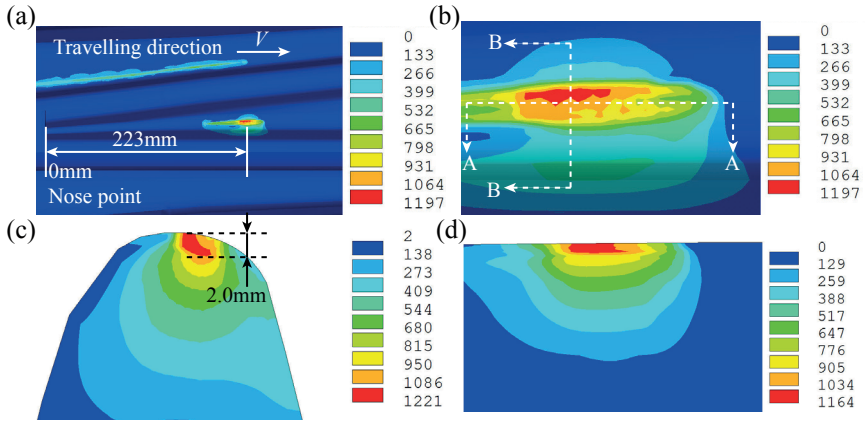

Figure 25: Distribution of subsurface Von-Mises stress (Unit:MPa): (a) Global view; (b) Close-up view; (c) Von-Mises stress on cutting plane "BB"; (d) Von-Mises stress on cutting plane "AA".

4.2.2. Shear stress

Figure 26a-b show the global view and close-up view of the shear stress in the longitudinal direction. As the wheel rolls, it can be seen from "AA" cutting plane as shown in Figure 26d that tensile shear stresses are created at the rear of the contact patch and compressive shear stresses at the front of the contact patch. For the shear stress mapped on the "BB" cutting plane as shown in Figure 26c, the shear stress is more concentrated on the right side of the nose rail than on the left side. This phenomenon can be caused by the unsymmetrical contact angle between wheel and crossing contact geometries.

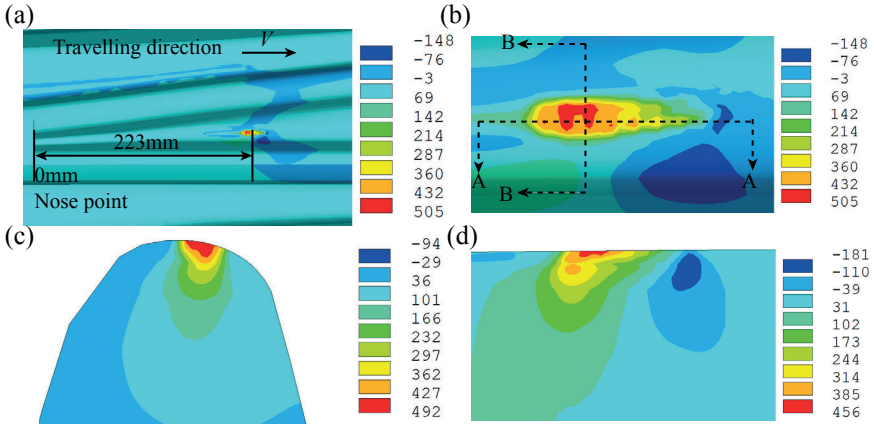

Figure 26: Distribution of subsurface shear stress (Unit:MPa): (a) Global view; (b) Close-up view; (c) Shear stress on "BB" cutting plane; (d) Shear stress on "AA" cutting plane.

4.3. Discussions of results & future work

The studies on the surface & subsurface stress responses demonstrate the influence of the dynamic impact on the material responses. Based on the FE simulation results, the causes of the rapid crossing surface degradation and the further model improvements & applications are discussed.

4.3.1. Causes of rapid surface degradation

The surface degradation is referred to as wear, plastic deformation, RCF cracks (e.g., spalling damages, See Figure 1), etc., which are commonly observed on the crossing rail.

From the results of contact forces (See Figure 21), it can be seen that the nominal axle load(100kN) has been drastically amplified more than 2 times (around 216.3kN). Accordingly, both the maximum local contact normal (2072MPa) and shear stresses (542MPa) (See Figure 22 and Figure 23) are increased accordingly around 2 times, in comparison to the case of normal wheel-rail interaction [38] (See Table 5). These impact-induced stresses (See Section 4.1 and Section 4.2) exceed the yield limit of the material (480MPa) greatly.

Considering the severe loading condition over one cycle, one might imagine that the processes of wear/RCF damage initiate in the microscopic scale. Under such cyclic loading condition, localized plastic deformation and/or cracks propagate proactively in the macroscopic scale. As a consequence, the rapid surface degradation in 1:9 crossing panel occurs.

4.3.2. Cons of 'eFE-CS' model: further improvement

Although the developed 'eFE-CS' model has been validated to be a reasonably accurate and reliable tool for studying the dynamic impact between wheel and crossing, there is still plenty room remained to increase its degree of realism and accuracy. For instance,

- ◇ To enhance the steering capability: In the present 'eFE-CS' model, the steering capability of the wheel is quite limited, since the yaw motion is not allowed and only roll motion is considered. For this reason, it is difficult to simulate the case of wheel-crossing dynamic impact at the diverging route. To study the more complex case of diverging route (See Figure 1a), it is motivated to introduce several torsional control units onto the wheel so as to enhance the steering capability.

- ◇ To take the stock rail into account: A complete wheel-set rolling over a crossing panel (including both crossing and stock rails) is to be modelled. By this means, the effects of the stock rail and second wheel of the axle on the dynamic impact phenomenon are able to be fully considered. It was reported in [16] that the complete modelling approach could simulate the dynamic impact with higher accuracy since it was much close to the real-life situation.

4.3.3. Future applications of 'eFE-CS' model

As it can be seen from the simulation results, the 'eFE-CS' model can provide detailed knowledge of stress/strain responses within the contact patches. This makes the proposed model attractive to use in advanced applications, wherein such information is needed. For instance,

- → To study the tribological responses under varying operational patterns: It has been reported in [38] that the variation of the operation patterns (friction coefficient, traction coefficient, etc.) can significantly influence the material responses in the case of normal wheel-rail interaction. Regarding the dynamic impact between wheel and crossing, the research interests are strongly excited so as to find the countermeasures to the specific types of surface damage, which are suspected to be the consequences of large shear stresses.

- → Real-time assessment of the functional state and maintenance demand of the in-situ wheel and/or crossing profiles: It is worth noting that all the procedures of the coupling strategy have been programmed and parametrised using MATLAB and ANSYS Parametric Design Language (APDL). Thus, the developed FE model can easily be adjusted for other wheel and rail properties (e.g. worn wheel and/or

crossing profiles). Based on the simulation results, it is helpful to make the decisions on whether to perform re-profiling, local grinding & welding and/or lubricating operations or not.

→ Profile design/optimisation: Given the properly parametrised profiles of crossing rail (Using spline or B-spline techniques), the validated FE model could be further extended as a tool for the profile design [3] and/or optimisation [1, 10].

→ Wear & RCF (service life) prediction: Using the well-established wear/multi-axial fatigue life models, the degradation process of the crossing rail, such as wear [47], rolling contact fatigue (RCF) crack initiation and propagation [48, 49], etc., can be predicted.

5. Conclusions

In this paper a three dimensional (3D) explicit finite element (FE) model of a wheel rolling over a 1:9 crossing rail has been developed. To address the associated FE modelling difficulties, a coupling strategy (called 'eFE-CS') that combines the two dimensional (2D) geometrical contact analyses has been proposed. The necessity of this coupling strategy has been investigated through the comparisons of FE simulated dynamic contact forces with those obtained from the 'conventional' FE model. Also, the accuracy of presented 'eFE-CS' model has been evaluated through effective experimental validations. The FE simulated stress solutions of dynamic impact at S&C have been presented. The further improvements and applications of the developed 'eFE-CS' model have been discussed. Based on the results and discussions, the following conclusions are drawn:

(1) The detailed working scheme of coupling strategy has been introduced with application to the analysis of wheel-crossing (W/C) dynamic impact. Using this strategy, both the general and specific W/C FE modelling difficulties (e.g., 'gaps and/or penetrations', 'smooth mesh transitions', etc.) have been addressed. The comparative study shows that the calculation efficiency can be significantly improved using the 'eFE-CS' strategy, which can reduce the amount of elements and increase the calculation time step size. In short, the 'eFE-CS' is quite effective to address the FE modelling problems of W/C dynamic impact and is, thus, recommended to use in the contact/impact systems that having complex local contact geometries.

(2) The validation of transition region estimated by the 'eFE-CS' model with the field measured one shows a good agreement at the starting point of the transition process. As for the ending point, the discrepancies between filed measured and FE predicted results are getting much noticeable. The sources of these discrepancies have been explained (e.g., multiple wheel passages, variable local contact geometries, etc.).

(3) The validation of crossing accelerations is performed from a statistical perspective. The results show that the magnitude of the impact accelerations from the FE model and the field measurements are comparable, while there are discrepancies observed. The sources of these discrepancies have been explained and categorised into different groups (such as, various operational patterns, unknown vehicle/track parameters, etc.). From these aforementioned experimental validations, it is worth noting that although the tolerable discrepancies exist, the FE results agree reasonably well with the field measurements.

(4) The stress results show that the validated 'eFE-CS' model is capable of providing a detailed rolling contact stress solution of dynamic impact at 1:9 crossing rail. At the most impacted moment, surface normal contact pressure can be 4 times higher than the yield limit. From the subsurface stress analysis, it finds that the high stress state is concentrated in a considerably small volume of material. As a result, the risk of surface degradation (i.e., crack initiation, plastic deformation, etc.) is significantly increased.

(5) As a major advantage of the 'eFE-CS' model, the detailed stress/strain solutions make it attractive to be used in other advanced applications (e.g., profile design/optimisation, Wear/RCF prediction, etc.). Also, there is plenty room left for further improving its degree of realism and accuracy (e.g., enhancing the steering capability, considering the multiple wheel passages, etc.).

Acknowledgements

The author Yuewei Ma would like to thank CSC (China Scholarship Council) for their financial support on part of this research. Special thanks goes to Dr. Hongxia Zhou for critically reading this manuscript and giving helpful suggestions. The authors are also grateful to Dr. Chang Wan (from Norwegian University of Science and Technology) and Dr. Xiubo Liu (from China Academy of Railway Sciences) for reading some parts of this manuscript and giving useful suggestions for improvement. The support of our colleague Mr. Xiangming Liu for sharing the acceleration data and photos is gratefully acknowledged. In addition, the authors would like to acknowledge Strukton Rail BV for providing the track location for measurements. Last but not least, the authors are very grateful to all the reviewers for their thorough reading of the manuscript and for their constructive comments.

References

[1] C. Wan, V. L. Markine, and I. Y. Shevtsov. Improvement of vehicle–turnout interaction by optimising the shape of crossing nose. *Vehicle System Dynamics*, 52(11): 1517–1540, 2014.

[2] A. Cornish, E. Kassa, and R. Smith. Field experimentation and analysis at switches and crossings in UK. In *CM 2012: 9th international conference on contact mechanics and wear of rail/wheel systems, 27- 30 August*, pages 649–651, Chengdu, China, 2012.

[3] A. A. Mashal. Analysis & improvement of railway crossing using explicit finite element method. Master of Science Thesis, Delft University of Technology, 2016.

[4] V. L. Markine and I. Y. Shevtsov. Experimental analysis of the dynamic behaviour of railway turnouts. In B.H.V. Topping, editor, *The 11th international conference on computational structures technology, 4 - 7 September*, pages 1–10, Dubrovnik, Croatia, 2012.

[5] X. Liu, V. L. Markine, and I. Shevtsov. Performance study of a double crossover for facing and trailing directions. In *IAVSD 2015: 24th International Symposium on Dynamics of Vehicles on Roads and Tracks, 17 - 21 August*, pages 1–9, Graz, Austria, 2015. CRC Press.

[6] E. Kassa and J. C. O. Nielsen. Stochastic analysis of dynamic interaction between train and railway turnout. *Vehicle System Dynamics*, 46(5):429–449, 2008.

[7] E. Kassa and J. C. O. Nielsen. Dynamic interaction between train and railway turnout: full-scale field test and validation of simulation models. *Vehicle System Dynamics*, 46(S1):521–534, 2008.

[8] S. Alfi and S. Bruni. Mathematical modelling of train–turnout interaction. *Vehicle System Dynamics*, 47(5):551–574, 2009.

[9] C. Wan and V. L. Markine. Parametric study of wheel transitions at railway crossings. *Vehicle System Dynamics*, 53(12):1876–1901, 2015.

[10] C. Wan, V. L. Markine, and I. Shevtsov. Optimisation of the elastic track properties of turnout crossings. *Proceedings of the Institution of Mechanical Engineers, Part F: Journal of Rail and Rapid Transit*, 230(2):360–373, 2016.

[11] M. Pletz, W. Daves, and H. Ossberger. A wheel passing a crossing nose: Dynamic analysis under high axle loads using finite element modelling. *Proceedings of the Institution of Mechanical Engineers, Part F: Journal of rail and rapid transit*, 226 (6):603–611, 2012.

[12] M. Pletz, W. Daves, and H. Ossberger. A wheel set/crossing model regarding impact, sliding and deformation - explicit finite element approach. *Wear*, 294:446–456, 2012.

[13] M. Wiest, E. Kassa, W. Daves, J. C. O. Nielsen, and H. Ossberger. Assessment of methods for calculating contact pressure in wheel-rail/switch contact. *Wear*, 265(9): 1439–1445, 2008.

[14] X. Shu, N. Wilson, C. Sasaoka, and J. Elkins. Development of a real-time wheel/rail contact model in nucars® 1 and application to diamond crossing and turnout design simulations. *Vehicle System Dynamics*, 44(sup1):251–260, 2006.

[15] A. Johansson, B. Pålsson, M. Ekh, J. C. O. Nielsen, M. K. A. Ander, J. Brouzoulis, and E. Kassa. Simulation of wheel–rail contact and damage in switches & crossings. *Wear*, 271(1):472–481, 2011.

[16] L. Xin, V. L. Markine, and I. Y. Shevtsov. Numerical analysis of the dynamic interaction between wheel set and turnout crossing using the explicit finite element method. *Vehicle System Dynamics*, 54(3):301–327, 2016.

[17] Z. H. Zhong and J. Mackerle. Contact-impact problems: A review with bibliography. *Applied Mechanics Reviews*, 47(2):55–76, 1994.

[18] E. A. H. Vollebregt. Numerical modeling of measured railway creep versus creep-force curves with contact. *Wear*, 314(1):87–95, 2014.

[19] E. Kassa and G. Johansson. Simulation of train–turnout interaction and plastic deformation of rail profiles. *Vehicle System Dynamics*, 44(sup1):349–359, 2006.

[20] Y. Bezin, I. Grossoni, and S. Neves. Impact of wheel shape on the vertical damage of cast crossing panels in turnouts. In Rosenberger M., editor, *IAVSD2015: 24th international symposium on dynamics of vehicles on roads and tracks, 17 - 21 August*, pages 1–10, Graz, Austria, 2015.

[21] B. A. Pålsson and J. C. O. Nielsen. Wheel–rail interaction and damage in switches and crossings. *Vehicle system dynamics*, 50(1):43–58, 2012.

[22] B. A. Pålsson. Design optimisation of switch rails in railway turnouts. *Vehicle System Dynamics*, 51(10):1619–1639, 2013.

[23] B. A. Pålsson. Optimisation of railway crossing geometry considering a representative set of wheel profiles. *Vehicle system dynamics*, 53(2):274–301, 2015.

[24] V. L. Markine, M. J. M. M. Steenbergen, and I. Y. Shevtsov. Combatting RCF on switch points by tuning elastic track properties. *Wear*, 271(1):158–167, 2011.

[25] I. Grossoni, Y. Bezin, and S. Neves. Optimization of support stiffness at a railway crossing panel. In Pombo J., editor, *Proceedings of the 3rd international conference on railway technology: Research, development and maintenance, 5 - 8 April*, pages 1–19, Cagliari, Italy, 2016.

[26] H. R. Hertz. Über die Berührung fester elastischer Körper und über die Härte. *Journal für die reine und angewandte Mathematik*, 92:156–171, 1882.

[27] J. J. Kalker. *Three-dimensional elastic bodies in rolling contact*, volume 2. Springer Science & Business Media, 1990.

[28] S. Bruni, A. Collina, G. Diana, and P. Vanolo. Lateral dynamics of a railway vehicle in tangent track and curve: tests and simulation. *Vehicle system dynamics*, 33 (Suppl.): 464–477, 2000.

[29] E. A. H. Vollebregt and P. Wilders. Fastsim2: a second-order accurate frictional rolling contact algorithm. *Computational Mechanics*, 47(1):105–116, 2011.

[30] O. Polach. Creep forces in simulations of traction vehicles running on adhesion limit. *Wear*, 258(7):992–1000, 2005.

[31] E. A. H. Vollebregt. User guide for contact, vollebregt & kalker's rolling and sliding contact model, techical report TR09-03, version, 2013.

[32] P. Wriggers and T. A. Laursen. *Computational contact mechanics*, volume 30167. Springer Science & Business Media, 2006.

[33] Z. Wei, C. Shen, Z. Li, and R. P. B. J. Dollevoet. Wheel–rail impact at crossings: Relating dynamic frictional contact to degradation. *Journal of Computational and Nonlinear Dynamics*, 12(4):041016, 2017.

[34] J. Wiedorn, W. Daves, U. Ossberger, H. Ossberger, and M. Pletz. Simplified explicit finite element model for the impact of a wheel on a crossing–validation and parameter study. *Tribology International*, 111:254–264, 2017.

[35] Y. Ma, V. L. Markine, A. A. Mashal, and Ren M. Improving performance of finite element simulations on wheel-rail interaction using a coupling strategy. *Proceedings of the Institution of Mechanical Engineers, Part F: Journal of Rail and Rapid Transit, (In Revision)*, 2017.

[36] X. Zhao and Z. Li. The solution of frictional wheel–rail rolling contact with a 3D transient finite element model: Validation and error analysis. *Wear*, 271(1):444–452, 2011.

[37] M. Molodova, Z. Li, A. Núñez, and R. Dollevoet. Validation of a finite element model for axle box acceleration at squats in the high frequency range. *Computers & Structures*, 141:84–93, 2014.

[38] Y. Ma, V. L. Markine, A. A. Mashal, and M. Ren. Modelling verification and influence of operational patterns on tribological behaviour of wheel-rail interaction. *Tribology International*, 114:264–281, 2017.

[39] Y. Ma, V. L. Markine, A. A. Mashal, and Ren M. Effect of wheel-rail interface parameters on contact stability in explicit finite element analysis. *Proceedings of the Institution of Mechanical Engineers, Part F: Journal of Rail and Rapid Transit, (In Revision)*, 2017.

[40] European Committee for Standardization (CEN) EN 13715: 2006 + A1. Railway applications – wheelsets and bogies – wheels – tread profile, 2006.

[41] International Union of Railways (UIC) Code: 515-1 OR. Passenger rolling stock - trailer bogies - running gear - general provisions applicable to the components of trailers bogies. Leaflet, 2003.

[42] J. O. Hallquist. ANSYS/LS-DYNA theoretical manual, 2005.

[43] ANSYS Inc. Ansys release 17.1, mechanical applications theory reference, 2016.

[44] P. Pütz. User manual ESAH-M v2.2., 2011.

[45] J. Tunna, J. Sinclair, and J. Perez. A review of wheel wear and rolling contact fatigue. *Proceedings of the Institution of Mechanical Engineers, Part F: Journal of Rail and Rapid Transit*, 221(2):271–289, 2007.

[46] K. L. Johnson. *Contact mechanics*. Cambridge university press, 1987.

[47] P. J. Blau. Embedding wear models into friction models. *Tribology Letters*, 34(1): 75–79, 2009.

[48] Y. Ma, V. L. Markine, and A. A. Mashal. Numerical analysis of rail surface crack propagation under cyclic rolling-sliding contact loads. In J. Pombo, editor, *Proceedings of the 3rd international conference on railway technology: Research, development and maintenance,5 - 8 April*, pages 1–14, Cagliari, Italy, 2016.

[49] Y. Ma, V. L. Markine, and A. A. Mashal. Rail surface crack initiation analysis using multi-scale coupling approach. In *IAVSD2015: 24th international symposium on dynamics of vehicles on roads and tracks, 17 - 21 August*, pages 1–10, Graz, Austria, 2015.